Atomic Scale Characterisation of Pt-Re/CeO_2 for the Water Gas Shift Reaction

Centre for Catalysis Research
Department of Chemical Engineering
University of Cape Town

Author: Richard B. Martin

Supervisor: Prof Patricia J. Kooyman

Submitted in partial fulfilment of the requirements for the degree of Master of Science in Chemical Engineering

March 2021

Plagiarism Declaration

I know the meaning of plagiarism and declare that all the work in the document, save for that which is properly acknowledged, is my own. This thesis/dissertation has been submitted to the Turnitin module (or equivalent similarity and originality checking software) and I confirm that my supervisor has seen my report and any concerns revealed by such have been resolved with my supervisor.

Name: Richard Martin
Date: March 2021
Signature:

Signed by candidate

Acknowledgements

I would like to acknowledge the help and support of my supervisor, Prof Patricia Kooyman for helping and guiding me through the process of creating this dissertation. I also thank you for the opportunities you have provided to me through exposure to international conferences and scientific collaboration. The extensive training for electron microscopy that you provided is invaluable.

The assistance of Dr Kinga Unocic and use of equipment at Oak Ridge National Laboratory, TN, USA is gratefully acknowledged for facilitating the *operando* work.

Financial support from the University of Cape Town and the DST-NRF Centre of Excellence in Catalysis (c*change) is gratefully acknowledged. This work is based on the research supported in part by the National Research Foundation of South Africa Grant number 94878 and 121235.

The use of the facilities and assistance provided by the Aaron Klug Centre for Imaging and Analysis at UCT is acknowledged. The assistance, training, and use of the facilities at the Centre for High Resolution Transmission Electron Microscopy at NMMU is also acknowledged.

A huge thank you goes to Ziba Rajan for her unwavering support, motivation, friendship, and source of many conversations that inspired helpful ideas for this work.

Finally, I would like to thank my family and friends for their support and motivation to keep me going throughout this process.

Conference Contributions

2018
R. Martin and P.J. Kooyman
"Atomic Scale Characterisation of Pt-Re/CeO_2 for the Water Gas Shift Reaction"
Poster presentation at IAMNano 2018, Hamburg, Germany.

R. Martin and P.J. Kooyman
"Atomic Scale Characterisation of Pt-Re/CeO_2 for the Water Gas Shift Reaction"
Poster presentation at the 29th Annual Conference of the Catalysis Society of South Africa (CATSA), Limpopo, South Africa.

R. Martin and P.J. Kooyman
"Atomic Scale Characterisation of Pt-Re/CeO_2 for the Water Gas Shift Reaction"
Poster presentation at the Microscopy in Material Science 2018 Workshop, Johannesburg, South Africa.

2019
R. Martin and P.J. Kooyman
"Atomic Scale Characterisation of Pt-Re/CeO_2 for the Water Gas Shift Reaction"
Poster presentation at the 30th Annual Conference of the Catalysis Society of South Africa (CATSA), Western Cape, South Africa.
R. Martin and P.J. Kooyman

"Refacetting of Platinum-Rhenium Nanoparticles Under Operando Water Gas Shift Conditions"
Oral presentation at the 56th Congress of the Microscopy Society of South Africa (MSSA), Western Cape, South Africa.

Abstract

Inexpensive hydrogen gas is needed to transition to a hydrogen based economy. For this to happen, economically feasible, large scale production of hydrogen gas is required. Currently, electrolysis is unable to meet this demand economically, so steam reforming of hydrocarbons (e.g. methane) is required to produce large volumes of hydrogen. To be used for mobile applications, such as in hydrogen fuel cells, the hydrogen fuel must be free of CO which is poisonous to the fuel cell catalyst. The water gas shift (WGS) reaction is used to convert CO and H_2O to CO_2 and H_2, cleaning the fuel stream and producing additional hydrogen.

A medium temperature shift catalyst, operating in a temperature range of 280 to 350 °C can be used to perform the WGS in one step, simplifying the complex two step process used industrially and enabling small scale hydrogen production. The catalytic material used for the medium temperature shift is platinum on a metal oxide support, such as CeO_2, however this is prone to deactivation by sintering. It has been shown in literature that the addition of Re enhances the activity and stability of the catalyst, however it requires close contact with the platinum for promotion to take place. Traditional impregnation methods are unable to guarantee this close contact due to the non-uniform distribution of both metals on the catalyst support. Colloidal synthesis methods provide a way to ensure the platinum and rhenium are in close contact with each other. Literature has reported a method to produce homogeneously alloyed Pt_3Re nanoparticles. It was hypothesised that using the colloidal method for synthesising Pt-Re/CeO_2 catalysts would improve the activity and stability over Pt-Re/CeO_2 catalysts synthesised by the traditional impregnation method.

In this study the method reported in literature was optimised for small metallic nanoparticles with a spherical shape, which could then be supported on CeO. The optimised method was used to produce Pt/CeO_2 and Pt-Re/CeO_2 catalysts, while incipient wetness impregnation was used to produce a Pt-Re/CeO_2 catalyst for comparison. These catalysts were physically characterised used X-Ray diffraction (XRD), inductively coupled plasma optical emission spectroscopy (ICP-OES), and transmission electron microscopy (TEM). *Operando* TEM was used to observe the Pt and Pt-Re nanoparticles under water gas shift conditions. The nanoparticles exhibited oscillations between facetted and spherical shapes, which was not present under normal TEM imaging conditions. The cause of these oscillations was attributed to the presence of reactive gases and elevated temperature. The catalytic performance of the catalysts was evaluated at 320 °C and 350 °C, and the Pt-Re/CeO_2 synthesised by the colloidal method had the largest activity of all the catalysts, however, it showed more deactivation at 320 °C than the Pt-Re/CeO_2 catalyst prepared by impregnation. At 350 °C, all of the catalysts showed an increase in stability.

In conclusion, Pt-Re/CeO_2 prepared by the colloidal method had a higher activity (at all temperatures) than Pt-Re/CeO_2 prepared by the impregnation method, due to the closer contact between Pt and Re, with increasing stability at higher temperatures, the cause of which is currently unknown.

Contents

List of Figures

List of Tables

Nomenclature

Abbreviation	
DI	Dry impregnation
fcc	face-centred cubic
FFT	Fast Fourier transform
GC	Gas chromatography
HTS	High temperature shift
ICP-OES	Inductively coupled plasma optical emission spectroscopy
IWI	Incipient wetness impregnation
LTS	Low temperature shift
MEMS	MicroElectroMechanical Systems
MFC	Mass flow controller
MTS	Medium temperature shift
PFD	Process flow diagram
PSD	Particle size distribution
PVI	Pore volume impregnation
SEM	Scanning electron microscopy
SPS	Solution phase synthesis
STP	Standard temperature and pressure
TEM	Transmission electron microscopy
ToS	Time on stream
TPR	Temperature-programmed reduction
WGS	Water gas shift
WI	Wet impregnation
XRD	X-Ray diffraction

Chapter 1

Introduction

The generation of hydrogen gas is vital for transitioning towards a low-carbon economy. The use of fossil fuels is responsible for the generation of greenhouse gases (e.g. excessive carbon dioxide) that are responsible for climate change (Bartels *et al.*, 2010). In addition to this, fossil fuels are non-renewable resources and reserves will eventually be depleted. It is estimated that the world currently has approximately 50 years of natural gas reserves, and 120 years of coal reserves (Bartels *et al.*, 2010).

Hydrogen generated from biofuels uses a similar process to that generated from fossil fuels (especially natural gas) and has the added benefit that biofuels are a renewable resource (Bartels *et al.*, 2010). Although biofuels can be utilised directly in mobile applications, such as bioethanol or biogas, this generates carbon dioxide and carbon monoxide that is very difficult to remove due to its low concentration per vehicle. Hydrogen generated from biofuels does emit carbon dioxide (carbon monoxide is reacted away during hydrogen generation), however this is a point source of carbon dioxide. The carbon dioxide can be sequestered or captured to provide pollutant free hydrogen.

The water gas shift (WGS) reaction is the process by which carbon monoxide and water are converted to carbon dioxide and hydrogen. Industrially, this is carried out in a large, two-step process, using two reactors with two different catalysts at different temperatures. A single stage water gas shift reactor operating between 280 and 350 °C is utilised to generate hydrogen for mobile applications, such as hydrogen fuel cells (Azzam *et al.*, 2007). This process requires a noble metal (e.g. Pt) catalyst supported on a metal oxide support (e.g. CeO_2) (Kalamaras *et al.*, 2011; Sato *et al.*, 2005).

While these catalysts are generally highly active, they are unstable and deactivate quickly. As platinum is a costly noble metal, this is not an ideal scenario. Rhenium has been reported as a promoter that improves the activity and stability of platinum supported on TiO_2 (Azzam *et al.*, 2008; Sato *et al.*, 2006; Radhakrishnan *et al.*, 2006), due to its co-location with platinum and potential alloying under WGS reaction conditions. The synthesis of platinum co-located with rhenium is difficult to achieve using traditional impregnation techniques (Ertl *et al.*, 1997). Colloidal methods have been shown to provide excellent control over nanoparticle size, shape, and composition (Munnik *et al.*, 2015), therefore such methods should be explored for WGS.

This study will investigate the synthesis of three catalysts via two different methods. Using colloidal synthesis, a platinum supported on ceria (Pt/CeO_2) catalyst, and a Pt-Re/CeO_2 catalyst were synthesised. For comparison, a Pt-Re/CeO_2 catalyst was synthesised via traditional impregnation techniques. These catalysts were characterised with transmission electron microscopy (TEM) and X-ray diffraction before being used for the WGS reaction. In addition,

operando TEM was used to study the Pt and Pt-Re nanoparticles over the course of the reaction. The WGS performance of the prepared catalytic materials was assessed to determine the synthesis method which resulted in the most active and stable catalyst. Post-run characterization was utilized to gain an understanding towards the changes which took place during the reaction.

Chapter 2

Literature Review

2.1 Hydrogen Generation for Energy

There is a large number of ways to generate hydrogen gas (e.g. steam reforming, electrolysis, coal gasification, pyrolysis) for use in a hydrogen fuel cell which generates electricity from hydrogen and oxygen gas (Bartels *et al.*, 2010). These are differentiated by the hydrogen and energy sources used respectively. The method used for hydrogen extraction has an impact on both the cost and the amount of pollution generated.

2.1.1 Hydrocarbon Sources

The generation of hydrogen from hydrocarbons (e.g. methane, ethane, pentane, coal) is similar in that the hydrocarbons are used as both a fuel to provide heat and as a source of hydrogen (Bartels *et al.*, 2010). The fuel is first reformed, using steam and heat, to produce a synthesis gas containing hydrogen, carbon monoxide, carbon dioxide, and water. This gas is then further processed using the WGS reaction to produce a hydrogen gas stream containing minimal amounts of carbon monoxide, which is poisonous to the platinum catalyst of the hydrogen fuel cell (Sato *et al.*, 2005).

An alternate source for the generation of hydrogen is water. This is done via the use of electrolysis, where electricity is used to power an alkaline, acidic, or solid oxide electrolyser that generates hydrogen and oxygen gas. These gases are then used in a hydrogen fuel cell to generate electricity (Bartels *et al.*, 2010). This process inherently generates no carbon monoxide or carbon dioxide which is advantageous to the operation of the hydrogen fuel cell and the environment.

2.1.2 Economics of Feedstock Choice

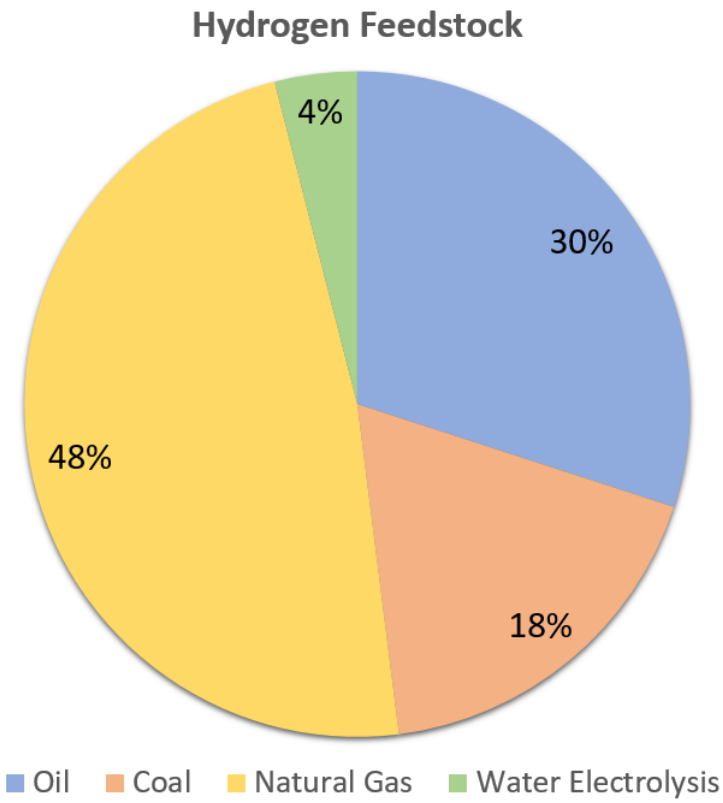

Figure 2.1: Feed stocks used globally for the generation of hydrogen. Adapted from Kothari *et al.* (2008)

As seen in figure 2.1, 96% of the world's hydrogen is generated by the use of hydrocarbons as feedstocks. Subsequently, the price of hydrogen generated from these sources is lower than hydrogen generated from electrolysis, mainly due to the economics of large-scale generation (Bartels *et al.*, 2010; Mueller-Langer *et al.*, 2007).

Table 2.1: Price of hydrogen across different types of energy sources, in 2007 US Dollars. Adapted from Bartels *et al.* (2010)

Source of Energy	Generation Method	Hydrogen Price ($/kg)
Coal	Gasification	0.3 - 1.83
Biomass	Gasification, Pyrolysis	1.25 - 2.83
Natural Gas	Steam Reforming	2.33 - 3.17
Wind	Electrolysis	2.27 - 6.77
Solar	Electrolysis	5.10 - 23.27

From table 2.1, the relationship between the price of hydrogen and the source used for generation is exemplified. Coal is the cheapest source to use for hydrogen generation, while solar produces the most expensive hydrogen and is unfavourable for hydrogen generation. Hydrogen generated from wind can be economically competitive with natural gas generation, but it cannot compete with coal and biomass. Between wind and solar there is a large price difference, showing that water electrolysis is heavily dependent on low cost electricity, in order to be competitive with hydrogen generated by hydrocarbon sources. Therefore, the energy effi-

ciency of electrolysis must be improved or fossil fuel prices must rise in order for the use of renewable energy sources in hydrogen generation to increase.

2.1.3 Environmental Impact

During the process of reforming fuels, carbon monoxide and carbon dioxide are generated. Carbon monoxide is reacted to carbon dioxide, which is a known greenhouse gas and should be avoided as much as possible (Bartels *et al.*, 2010). However, the release of carbon dioxide into the atmosphere could be mitigated by the addition of a carbon dioxide removal system to the WGS unit. This also has the benefit of improving the equilibrium conversion towards the reactants, eliminating the need for additional methods for the removal of carbon monoxide (Azzam *et al.*, 2007).

On the other hand, electrolysis does not generate any carbon monoxide or carbon dioxide during the process of splitting water. It is however, dependent on electricity, and the generation of this electricity can therefore be a significant source of pollution during the process. Carbon-free electricity, such as that from renewable energy sources (wind, solar, geothermal, hydroelectric, etc.) or nuclear power can be used to provide electricity instead of coal, oil or natural gas fired power plants that generate carbon dioxide and other pollutants (Bartels *et al.*, 2010).

2.1.4 Justification for the Water Gas Shift Reaction

The generation of hydrogen from a hydrocarbon source does produce greenhouse gases, mainly in the form of carbon dioxide. However, this can be removed using carbon capture and storage technology. Carbon capture and storage can be achieved in many ways including absorption (e.g. Selexol or Rectisol processes); adsorber beads made from alumina, a zeolite, or activated carbon; regenerative pressure or temperature swing adsorption; or membrane separation (e.g. using a polydimethylsiloxane membrane) (Rubin *et al.*, 2012). The price of generating hydrogen using hydrocarbons is cheaper than using electrolysis, which is heavily dependent on the price of electricity. Therefore, using a combination of reforming and WGS technology is required to economically generate the large volumes of hydrogen needed to transition to a hydrogen based economy.

2.2 The Water Gas Shift Reaction

The WGS reaction (see equation 2.1) is used industrially to reform synthesis gas (syngas) by reducing the amount of carbon monoxide present and increasing the amount of hydrogen generated. This is done by reacting carbon monoxide with water to form hydrogen and carbon dioxide. This is useful as it removes catalytically poisonous carbon monoxide and increases the amount of hydrogen available for further reaction, e.g. in a hydrogen fuel cell or for ammonia production (Azzam *et al.*, 2007; Choung *et al.*, 2005; Sato *et al.*, 2005, 2006).

$$CO_{(g)} + H_2O_{(g)} \leftrightarrow CO_{2(g)} + H_{2(g)} \quad \Delta H = -41.2kJ/mol \tag{2.1}$$

2.2.1 Modes of Operation

As the WGS reaction is mildly exothermic and equilibrium limited (an increase in temperature reduces the hydrogen yield), it is carried out in two stages industrially (Gonzalez Castaño *et al.*, 2014). The first step is the high temperature shift (HTS), followed by the low temperature shift (LTS). The HTS is carried out between 350 and 450 °C, and the LTS is carried out between 180 to 230 °C (Sato *et al.*, 2005). For the HTS, an iron-chromium mixed oxide (Fe_2O_3/Cr_2O_3) is

used, while a copper and zinc oxide supported on alumina ($Cu/ZnO/Al_2O_3$) is used for the LTS (Azzam *et al.*, 2008; Gonzalez Castaño *et al.*, 2014).

A medium temperature shift (MTS) catalyst operates between the temperatures of the HTS and the LTS. It usually consists of a noble metal (e.g. Pt) supported on a metal oxide support (Azzam *et al.*, 2007). The process can be simplified down to a single reactor because the metal is more active than iron and more resistant to sulphur and high temperatures than copper (Azzam *et al.*, 2007). Although the MTS uses costly noble metals, these are generally loaded onto the support in the range of 1 to 2 wt % (Sato *et al.*, 2006). These catalysts are more active than HTS and LTS systems, so less of it is needed and it could potentially scale down towards hydrogen generation for hydrogen fuel cells in vehicles (Sato *et al.*, 2005).

2.3 Design of a Medium Temperature Shift Catalyst

A robust and efficient MTS catalyst should be highly active and stable over long periods of operation. To this end, careful consideration must be taken towards the choice of active metal and the support material used for the catalyst.

2.3.1 Selection of Pt as the Active Metal

Platinum, palladium, and iridium have been identified as a potential alternative WGS catalysts (Sato *et al.*, 2005; Gonzalez Castaño *et al.*, 2014), with platinum having a few advantages over the other metals.

Platinum is active at low temperatures (minimum 100 °C) and can also be exposed to higher temperatures (maximum 400 °C) while being active for the WGS reaction. However, Pt catalysts are prone to degradation phenomena, such as sintering (Azzam *et al.*, 2007; Sato *et al.*, 2005). Sato *et al.* (2006) have studied the differences between platinum, palladium and iridium for the WGS reaction, all of which were supported on titania. The WGS reaction was evaluated at a temperature of 100 °C for the platinum and iridium catalysts, while the palladium catalyst was evaluated at a higher reaction temperature of 200 °C. As palladium is inactive for the WGS reaction at 100 °C, and only mildly active at higher temperatures, it is not a suitable candidate. Sato *et al.* (2006) did not state why they did not assess the platinum and iridium catalysts at 200 °C as well, as this would have served as a better comparison against the palladium. It was found that platinum had a higher WGS activity than iridium.

Due to its higher activity than palladium and iridium, and its greater resistance to sulphur than copper (Azzam *et al.*, 2007), platinum is a suitable metal for use in medium temperature shift conditions.

2.3.2 Selection of CeO_2 as the Support

The selection of a support is crucial in the water gas shift reaction, as it stabilises the metal by preventing sintering, and metal-support interactions enhance the catalytic performance (Vignatti *et al.*, 2010). CeO_2, TiO_2, ZrO_2, and SiO_2 have all been used as supports for Pt metal nanoparticles (Sato *et al.*, 2006; Azzam *et al.*, 2007; Vignatti *et al.*, 2010). Vignatti *et al.* (2010) compared the activity of Pt supported on CeO_2, SiO_2, and TiO_2, and found that platinum supported on CeO_2 performed better than platinum supported on SiO_2, due to SiO_2 being inert towards WGS and not enhancing the catalytic activity. Platinum supported on TiO_2 is more active than platinum supported on CeO_2 due to platinum enhancing the reducibility of TiO_2

and the catalytic activity towards WGS, but is more prone to deactivation by support sintering (Vignatti *et al.*, 2010; Kalamaras *et al.*, 2011). Therefore, selecting CeO_2 as a support offers increased activity over SiO_2 and higher stability than TiO_2 and it is a suitable candidate for further research.

2.3.3 Addition of Re as a Promoter

Due to instability of platinum supported on CeO_2 at high temperatures, investigations (Azzam *et al.*, 2008; Sato *et al.*, 2005, 2006; Del Villar *et al.*, 2016; Radhakrishnan *et al.*, 2006; Choung *et al.*, 2005) have been conducted on the addition of rhenium to determine its efficacy as a catalytic promoter. Rhenium was found by Del Villar *et al.* (2016) and Azzam *et al.* (2008) to reduce the amount of platinum needed to achieve the same activity as unpromoted platinum, while also increasing the catalytic stability. The mechanism of promotion is not fully understood yet, as the WGS reaction mechanism differs depending on which oxide support is used in the catalyst (Azzam *et al.*, 2008; Sato *et al.*, 2006; Vignatti *et al.*, 2010).

Importantly, pure rhenium has been found by Choung *et al.* (2005) to be inactive for the WGS reaction at temperatures lower than 350 °C, and only slightly active at 400 °C using a $Ce_{0.46}Zr_{0.54}O_2$ support. Temperatures below 350 °C are used for MTS WGS technology, so pure rhenium has no WGS activity in the MTS temperature range.

The effect of rhenium promotion on platinum, palladium and iridium WGS catalysts was investigated by Sato *et al.* (2006), where it was found that platinum maintained the highest activity compared to palladium and iridium. Figure 2.2 shows the effect of increasing rhenium content for the promotion of platinum, iridium, and palladium WGS catalysts. Palladium was evaluated at a higher temperature than the platinum and iridium, thus no direct comparison can be made. Platinum had a higher WGS activity than iridium at all rhenium loadings. Figure 2.2 demonstrates that even a low loading of rhenium should be sufficient to see a significant improvement in catalytic activity.

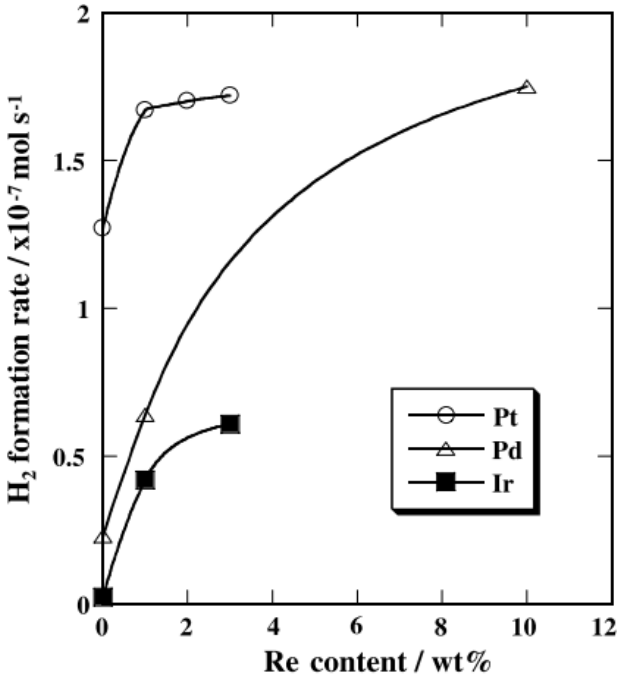

Figure 2.2: Dependence of H_2 formation rates of the WGS reaction on Re content within 2 wt % Pt–Re/TiO_2 (100 °C), 1 wt % Pd–Re/TiO_2 (200 °C) and 1 wt % Ir–Re/TiO_2 (100 °C). Source: Sato *et al.* (2006).

2.4 Water Gas Shift Mechanism over Metal Oxide-Supported Pt Catalysts

The WGS reaction can occur through two reaction pathways - that of the formate (associative) mechanism, with the other reaction pathway being the redox (regenerative) mechanism, depending on the support chosen (Azzam *et al.*, 2008; Sato *et al.*, 2005; Kalamaras *et al.*, 2011).

The associative mechanism uses adsorbed species (formates) to carry out the WGS reaction. This is where water dissociatively adsorbs onto the surface to form OH and H species. The OH species react with the adsorbed CO to form HCOO, which then decomposes into carbon dioxide and hydrogen, which then desorb from the catalyst (Sato *et al.*, 2005).

The redox mechanism involves the successive reduction (by CO) and then oxidation by water of the support, according to Azzam *et al.* (2008). Sato *et al.* (2005) explain the redox mechanism differently - here it is said that water dissociatively adsorbs onto the surface as O and H species. The CO then reacts with the O to form carbon dioxide, while the two remaining hydrogen species form hydrogen gas. Both groups note that the mechanism is complex and that the dominant route is determined by the choice of catalyst support.

Azzam *et al.* (2008) suggest that in Pt/TiO_2 catalysts, an associative mechanism with redox regeneration is also a possibility for the WGS reaction. In this mechanism, lattice oxygen from the oxide support reacts with adsorbed carbon monoxide to form carbon dioxide. Water would then adsorb associatively onto the reduced support surface, regenerating the support via oxidation, and directly causing the desorption of hydrogen in one step. In their previous work Azzam *et al.* (2007), found that the WGS reaction takes place via both the redox and the asso-

ciative formate routes.

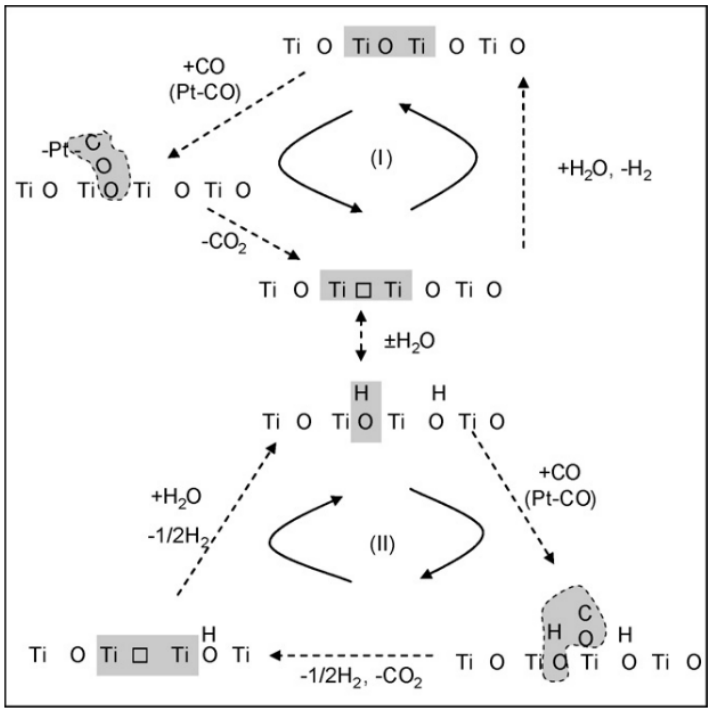

Figure 2.3: Water gas shift reaction mechanism on a Pt/TiO_2 catalyst. I: redox cycle. II: Formate with redox regeneration of the oxide. Source: Azzam *et al.* (2008).

The mechanisms of reaction for WGS on TiO_2 are shown in figure 2.3; this illustrates the role of the metal oxide support in the catalytic cycle, and explains how the choice of support can influence the reaction to a significant extent. The active role of the support provides insight as to why the stability of the catalyst is low at high temperatures - the increased reaction rate leads to sintering due to the large amount of heat being released from adsorption of carbon monoxide and water, and partial WGS reaction on the surface of the support. Sintering would then lead to larger particle size, therefore losing surface area available for reaction.

The associative mechanism with redox regeneration was suggested by Azzam *et al.* (2007) to be the main route by which the WGS reaction occurs on any metal oxide support, not just titania. This was found by Kalamaras *et al.* (2011) to be true to a certain extent with platinum supported on ceria. Kalamaras *et al.* (2011) concluded that the dominant mechanism was the redox route, and that the associative route also occurred, but to a lesser extent. Bunluesin *et al.* (1998) conducted a similar study to Kalamaras *et al.* (2011), and proposed that the oxygen transfer from the ceria support to the metal catalyst, together with the re-oxidation of the support by water, controlled the overall WGS reaction rate.

2.4.1 Changes to the WGS Mechanism with Re Addition

When platinum is promoted with rhenium, the increase in activity and stability cannot only be attributed to an increase in dispersion, but also a mechanistic change of the WGS reaction. The formation of bimetallic Pt-Re clusters was claimed to be observed by Sato *et al.* (2005) due to the presence of slightly negatively charged Pt (compared to Pt^0) and slightly positively charged Re in the XPS results. It was also found that the addition of 10 Torr of water at 100 °C caused a positive shift in the Re binding energy of 0.4 eV, while the Pt binding energy did not shift as

much, indicating oxidation of surface Re by the water.

Azzam *et al.* (2008) found that rhenium was not present in the form of Re^0 next to the platinum, but rather as ReO_x particles, at a reaction temperature of 300 °C. It was found that the ReO_x particles could not be fully reduced at these reaction conditions. This irreducibility of the ReO_x particles is supported by the work of Del Villar *et al.* (2016), who ran a temperature-programmed reduction (TPR) study of Pt-Re/CeO_2-TiO_2, and found a peak at 337 °C that corresponded with the reduction of ReO_x. Azzam *et al.* (2008) then attributed the promotion effect of ReO_x to its ability to provide another redox pathway for WGS, where the CO adsorbed on platinum partially reduces the ReO_x, yielding ReO_{x-1} and CO_2, which is then oxidised by water to yield H_2 gas and ReO_x once more. It was concluded that the overall WGS mechanism on Pt-Re/TiO_2 was a combination of the associative route with redox regeneration via the metal oxide support, along with two redox routes that use TiO_2 and ReO_x. It was also concluded that the associative route with redox regeneration was the dominant pathway, with the rate limiting step being the adsorption of CO and subsequent reaction with the OH species on the metal oxide support. This work is in partial agreement with the study done by Sato *et al.* (2005), where it was proposed that the rate limiting step was adsorption of all species onto the catalyst. The reaction temperature investigated in Sato *et al.* (2005) varied between 100 and 250 °C, therefore this temperature difference may have affected the conclusion of each study.

2.4.2 Bimetallic Pt-Re Cluster Formation

As previously mentioned, it has been suggested by Sato *et al.* (2005, 2006); Choung *et al.* (2005), and Del Villar *et al.* (2016) that one of the ways in which rhenium promotes platinum is by bimetallic cluster formation. In this formation, the rhenium deposits next to the platinum, in close contact, forming an interface where the mechanism of promotion can occur. These bimetallic clusters help to increase the dispersion of the platinum, but it is well-agreed upon in literature that this is not the only reason for the increase in activity.

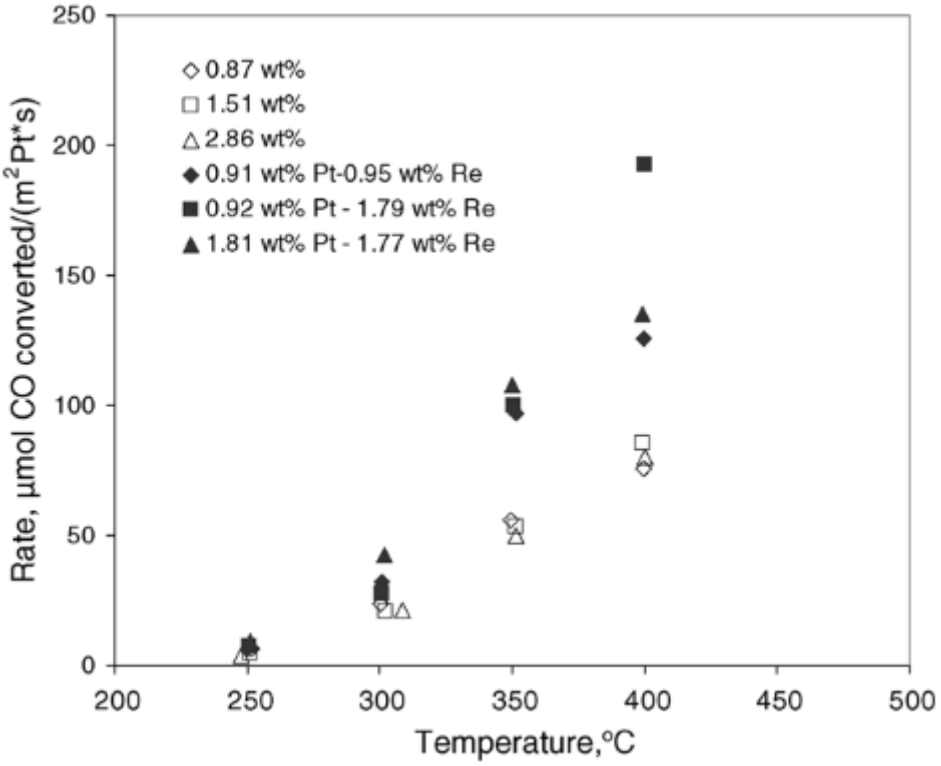

Figure 2.4: "Comparison of the WGS activity (per m^2 of Pt) of $Pt/Ce_{0.6}Zr_{0.4}O_2$ and $Pt-Re/Ce_{0.46}Zr_{0.54}O_2$ at various Pt weight loadings." Open shapes represent Pt catalysts, closed shapes represent Pt-Re catalysts. Source: Choung *et al.* (2005)

In a study conducted by Choung *et al.* (2005), it was noted that a significant increase in activity occurred upon addition of rhenium to platinum, supported on mixed cerium-zirconium oxides. Figure 2.4 shows the activity of the platinum and platinum-rhenium catalysts in the above mentioned study. Here, it is seen that Pt catalysts which did not contain rhenium generally exhibited a lower CO conversion than those that did contain rhenium. While it was observed that the presence of rhenium provided an enhancement in the dispersion of Pt nanoparticles over the oxide support, the WGS activity in this study was normalized with respect to the surface area of platinum, suggesting that the increase in activity could not be simply explained by the presence of rhenium increasing the dispersion of the Pt particles.

2.5 Synthesis Methods for a Medium Temperature Shift Catalyst

Bimetallic catalysts are conventionally prepared by impregnation methods Munnik *et al.* (2015); Vignatti *et al.* (2010); Azzam *et al.* (2007); Sato *et al.* (2006). While these techniques are simple and convenient, they have been shown to result in catalysts that are inhomogeneously distributed over the support material, with a broad particle size distribution (Ertl *et al.*, 1997; Ponec & Bond, 1995). When rhenium was deposited on its own (i.e. not co-located with platinum), it was found to be inactive towards the WGS reaction (Azzam *et al.*, 2008); therefore the deposition of isolated Re particles over the support leads to inefficient use of the precious metals (Pt, Re) present in the catalytic materials. An alternative catalyst synthesis method that produces homogeneously alloyed platinum and rhenium is therefore desired.

2.5.1 Impregnation Methods

Impregnation of a support with a metallic salt followed by a drying step is frequently used as a method for catalyst preparation, due to its ease of use (Munnik *et al.*, 2015). First, a soluble metal precursor (e.g. a nitrate, chloride, sulphate) is dissolved to concentrations below the solubility limit to ensure that no recrystallisation occurs before it is contacted with the support. Water is commonly used as a solvent, however, organic solvents can be used for water-insoluble salts, such as organo-metallics.

The next step can differ depending on which impregnation method is used. There are two main methods: wet impregnation (WI), which uses an excess of solution, and incipient wetness impregnation (IWI), where the solution volume used matches the total pore volume of the support (Munnik *et al.*, 2015). IWI is also known as pore volume impregnation (PVI) or dry impregnation (DI). In IWI, the metal loading is directly controlled by the concentration of the solution added. If a loading is required that is higher than the solubility limit of the metal salt, multiple depositions will be required.

The impregnated support is dried at mild temperatures (below the decomposition temperature of the metallic salt) in order to increase the concentration of the metallic salt in solution past the solubility limit and force nucleation and crystallisation of the metal salt out of solution. As there are many nucleation sites provided by the support, this can occur anywhere on the support (Munnik *et al.*, 2015). In the case of synthesising alloys, it is not guaranteed that both metals will deposit in close proximity, as the two metal salts have no driving force to precipitate out of solution near each other, and can therefore form inhomogeneous distributions (Ertl *et al.*, 1997).

The final steps are calcination and reduction. Calcination in air at temperatures higher than 300 °C will oxidise the ligands of the metal salts, oxidise the metals, forming metal oxides, and most importantly fortify the active metal and support interactions. The resulting metal oxides are usually inactive for most catalytic reactions, and so therefore need to be converted to the metallic form. This is done by reduction of the metal oxide, usually by hydrogen in an inert gas, at the temperature required to reduce the metal. This temperature differs depending on which metal oxide is present.

2.5.2 Colloidal Synthesis

Colloidal synthesis is done by nucleating metal nanoparticles out of a liquid solution, forming a colloidal suspension. This suspension is then mixed with the catalyst support so that the metallic nanoparticles can migrate onto the support. This method allows for a greater control over the size and shape of the nanoparticles produced, as the particles are formed by an initial nucleation burst and then grow from the remaining precursor which is left in solution (Munnik *et al.*, 2015). The period of time allowed for growth, and the temperature affect the size and shape of the resulting nanoparticles. Surfactants are added to the mixture (e.g. oleic acid) to help prevent the coalescence of the nanoparticles. Capping agents can be used to control the shape of the nanoparticles if needed (Munnik *et al.*, 2015).

The production of homogeneous alloys is in theory more feasible with colloidal synthesis than with an impregnation method, as the only place for metals to nucleate is on each other after the initial nucleation burst. Raciti *et al.* (2016) reported a synthesis of Pt_3Re nanoparticles supported on carbon for the electrocatalytic reduction of oxygen. It was found that the resulting nanoparticles formed a homogenous alloy of platinum and rhenium, via a simple method which could easily be reproduced in a conventional laboratory setting. In addition, the surfac-

tants used, oleic acid and oleylamine, were found to have been easily removed by calcination at 185 °C. This method is therefore one that could be used as an alternative to IWI methods for the synthesis of oxide-supported Pt-Re WGS catalysts.

Chapter 3

Research Approach

3.1 Summary of Key Literature Findings

Pt/CeO_2 is a suitable alternative to the current copper and iron based catalysts used for the water gas shift reaction. However, while it is more active it is also unstable, which reduces the cost-effectiveness of the platinum metal. When rhenium is added to platinum, it improves the activity and stability of the catalyst by altering the water gas shift mechanism. In order to do this, it must be co-located or alloyed with the platinum metal. Traditional impregnation methods have poor control over where metals are placed, so an alternative synthesis method, such as colloidal synthesis should be investigated. Colloidal synthesis had previously been demonstrated to be able to produce Pt_3Re alloyed nanoparticles which could then be deposited on a support.

3.2 Hypothesis

Pt-Re nanoparticles produced by colloidal synthesis and deposited on ceria will have a greater activity and stability than a Pt-Re catalyst synthesised via an incipient wetness impregnation technique.

3.3 Objectives

- Synthesise, via a colloidal method, a Pt/CeO_2 catalyst and a Pt-Re/CeO_2 catalyst
- Synthesise, via incipient wetness impregnation, a Pt-Re/CeO_2 catalyst
- Characterise the freshly prepared catalysts
- Evaluate the performance of each catalyst for the water gas shift reaction
- Observe the metallic nanoparticles using *operando* TEM techniques
- Characterise the catalysts after having been evaluated under water gas shift conditions

3.4 Key Questions

1. Are bimetallic clusters of platinum and rhenium present on the catalysts?
2. Does rhenium improve the performance of platinum for the water gas shift reaction?
3. Does the method of synthesis affect the performance of the catalyst?

Chapter 4

Experimental

4.1 Solution Phase Synthesis

This synthesis method was originally taken from Raciti *et al.* (2016), however, it was found during analysis of the nanoparticles to have a large particle size distribution and irregular shapes when reproduced. The method was modified, and is presented below. The details of this modification are explained in chapter 5.

For this synthesis method, the chemicals used are listed in the table below:

Table 4.1: List of chemicals used for Solution Phase Synthesis

Chemical Name	Information	CAS Number	Supplier
Platinum acetylacetonate	≥99.98% pure	15170-57-7	Merck
Dirhenium decacarbonyl	98% pure	14285-68-8	Merck
Tungsten hexacarbonyl	99.99% pure	14040-11-0	Merck
Dibenzyl Ether	purum, ≥ 98%	103-50-4	Merck
Oleic acid	90% (technical grade)	112-80-1	Merck
Oleyl amine	70 % (technical grade)	112-90-3	Merck
Ethanol	99.9% AR Grade	64-17-5	Kimix
Hexane	99.9 % AR Grade	110-54-3	Kimix
Toluene	99.9 % AR Grade	108-88-3	Kimix
Cerium oxide	Nano powder, <100 nm, 99.95 %	1306-38-3	Merck

4.1.1 Synthesis Procedure

The Solution Phase Synthesis (SPS) of the nanoparticles was carried out in a round-bottom three-neck flask with a capacity of 50 mL. The flask was first loaded with 1 mmol of platinum acetylacetonate and 1 mmol of dirhenium decacarbonyl, and a Teflon coated magnetic stirring bar was added. The flask was then attached to a retort stand, and filled with 10 mL of dibenzyl ether, 1 mL of oleic acid, and 1 mL of oleylamine. A glass condenser was fitted to the middle neck and attached to the retort stand and cooled with tap water. A glass bath approximately half-full of silicon oil was placed on top of a hot-plate with magnetic stirring capabilities. The flask was lowered into the silicon oil bath until the silicon oil was above the level of the liquid in the flask. One of the necks on the side was sealed with a glass stopper. A tube with flowing argon gas at 2 bar was inserted through a rubber bung and through the third neck. The top of the glass condenser was left open so that the argon could flow freely through the setup. A thermocouple attached to the hotplate was inserted into the silicon bath to provide temperature control.

The hotplate temperature was set to 160 °C, and the stirring to 400 rpm. When the silicon bath reached the set-point of 160 °C, the glass stopper was removed, and 0.1 g (0.3 mmol) of tungsten hexacarbonyl was added to the flask with the help of a funnel, and the stopper re-inserted. The mixture was aged for 10 minutes, after which the flask was lifted up out of the silicon bath. Approximately 90 mL of ethanol was added to the flask to cool the suspension and flocculate the nanoparticles. The suspension was then emptied into a 100 mL beaker.

The suspension was divided into centrifuge tubes, with ethanol being used to balance the tubes. These tubes were centrifuged at 8000 rpm for 10 minutes. The supernatant was discarded. Hexane was added to the centrifuge tubes to re-disperse the nanoparticles. To support the nanoparticles on ceria at 1 wt% loading, the ceria was added to a beaker, along with the nanoparticles suspended in hexane. Toluene, equal in volume to the hexane, was added to the beaker, and the beaker was ultrasonicated for 1 hour. The catalyst was left to dry in a fume hood for 2 hours before being dried overnight in an oven at 60 °C. The surfactants remaining on the nanoparticles were removed by calcination in flowing air at 190 °C for 12 hours, with a temperature ramp rate of 2 °C/min. This lower calcination temperature of 190 °C (as opposed to the 350 °C used for the IWI catalyst) was used to ensure that the metallic nanoparticles did not oxidise and change shape from when they were synthesised.

4.2 Incipient Wetness Impregnation

The IWI method was used to prepare a Pt-Re/CeO_2 catalyst. The chemicals used are listed in the table below:

Table 4.2: Chemicals used for Incipient Wetness Impregnation

Chemical	Information	CAS Number	Supplier
Tetraamineplatinum (II) nitrate	99.995 % pure	20634-12-2	Merck
Ammonium perrhenate	$\geq$99 % pure	13598-65-7	Merck
Cerium oxide	Nano powder, <100 nm, 99.95 %	1306-38-3	Merck

4.2.1 Pore Volume Measurement

Dry ceria (as received) was weighed out and had a mass of 3.113 g. Distilled water was then added drop wise with thorough mixing in between each drop until the point of incipient wetness was reached. The wet ceria was then weighed, and had a mass of 3.991 g. The mass of water in the pores was 0.878 g, and had a volume of 0.878 mL, assuming a density of 1 g/mL for water. Therefore the pore volume is 0.282 mL/g of ceria.

4.2.2 Synthesis Procedure

A mass of 2.5 g for ceria, with a nominal Pt-Re (3:1, atomic) metal loading of 1 wt % was targeted. Dry ceria was weighed out with a mass of 2.47566 g. Then, tetraamineplatinum (II) nitrate was weighed out with a mass of 38.29 mg, and ammonium perrhenate was weighed out with a mass of 10.70 mg. Using a pore volume of 0.282 mL/g_{CeO_2}, the metal salts were dissolved in 0.6 mL of distilled water. The metal salt solution was added to the ceria and mixed thoroughly. The impregnated ceria was left in a 60 °C oven to dry overnight. It was then calcined at 350 °C (in order to decompose the metal salts) in flowing air for 12 hours, with a ramp rate of 2 °C/min.

4.3 Characterisation Techniques

4.3.1 X-Ray Diffraction

The fresh catalysts were analysed using powder X-ray diffraction (XRD). A Bruker D8 Advance diffractometer operating at 40 kV, equipped with a Co-K_α source (λ=1.78897 Å) was used to collect diffractograms of each catalyst. The $2\theta°$ collection range was between 20 and 120°, with a step size of 0.043003 ° and a dwell time of 6 s, each scan took 4 hours to complete.

XRD operates on the principle of constructive interference between monochromatic X-rays and a crystalline sample, and is governed by Bragg's law. Bragg's law relates the angle of incident X-rays with the angle of reflectance, with only constructively interfering X-rays reflecting at the same angle of incidence and be detected. The destructively interfering X-rays are not detected.

$$\lambda = 2d \sin\theta \tag{4.1}$$

Equation 4.1 represents Bragg's Law, where:

- λ is the incident X-ray's wavelength
- d is the spacing of the crystal lattice
- θ is the incident angle

Using Bragg's law, and knowing the angle at which the peak is detected at, the lattice spacing, or d-spacing can be obtained. Each crystal phase has unique set of d-spacings, which can be used for phase identification.

4.3.2 Transmission Electron Microscopy

Transmission electron microscopy (TEM) was the main method used to characterise the catalysts. It is able to provide information on the nanoparticle size and shape, as well as the locations of the nanoparticles within the support.

A TEM uses a high energy beam of electrons with uniform intensity transmitted through a thin specimen to produce a monochromatic image. This transmission projects 2D images of 3D materials, so essentially all the information is averaged through the sample and there is no depth to the image (Williams & Carter, 2009). Thus, care must be taken when interpreting the image so as to not create false impressions. Electrons will interact with the sample, generating an image. This interaction has a probability to scatter some electrons, while the majority will pass through the sample if it is thin enough. Elastically scattered (i.e. losing no energy from interaction with the sample) electrons are used to form images in either a bright field or dark field mode. In bright field mode, contrast is created mainly through the thickness and density variations within the sample, with thicker areas appearing darker than thinner areas. Diffraction in the sample can also lead to contrast. In dark field mode, contrast is created through the phase of the sample, with higher atomic numbered elements appearing brighter in comparison to lower atomic numbered elements. This phase contrast is also present in bright field mode to a lesser extent, usually requiring a greater difference in the atomic number in order to generate noticeable contrast in the image compared to dark field imaging.

For TEM imaging, a Tecnai F20 CRYO FEGTEM and a JEOL JEM-ARM200F double Cs-corrected STEM were used, both having an accelerating voltage of 200 kV.

TEM grids were prepared by taking samples of the nanoparticle suspensions and dropping them directly onto a QUANTIFOIL® TEM grid.

4.3.3 Image Analysis

The unsupported nanoparticles were imaged using TEM and particle size distributions (PSDs) were generated from these images. To analyse a large number of particles in a short period of time, ImageJ software was used to process the images. First, the images were filtered using a Gaussian filter with a radius of 0.8 nm, and then thresholded, using the Otsu function. The thresholded images then had watershedding applied to them to separate clustered particles from each other. The particle analyser tool was then used to measure the area of each particle, with areas smaller than 4 nm^2 excluded to ensure artefacts were not included in the final distribution. The areas of each particle were then converted to the particle equivalent diameter, binned and normalised to produce a histogram showing the PSD. In the histogram, μ is used to represent the average particle diameter, with σ representing the standard deviation, and n being the number of particles analysed.

Fast Fourier Transforms (FFTs) were also used on the high magnification TEM images where the atomic columns of the nanoparticles could be seen. This was also done using ImageJ. The FFTs allowed the d-spacing, and thus the phase of the material present, to be identified.

4.3.4 Operando TEM

The TEM operates at a vacuum within the column, as any gas present will interact with the electron beam and cause a loss of resolution. However, a catalytic reactor is not operated at vacuum pressures, with pressures ≥ 1 atm used industrially. Therefore, catalysts studied using conventional TEM are essentially frozen when analysed (i.e. no active reaction is taking place) due to the lack of atmosphere/reactive gases present, as well as the temperature being too low to activate a reaction on the surface of the catalyst. In order to gain insight into structural-activity relationships, simultaneous high pressure, high temperature, and high resolution imaging are required during the reaction.

In order to achieve this, a nanoreactor is used. This is a small reactor that can fit inside a TEM holder, and has the ability to heat the catalyst and flow reactive gases over it, while being observed using the TEM.

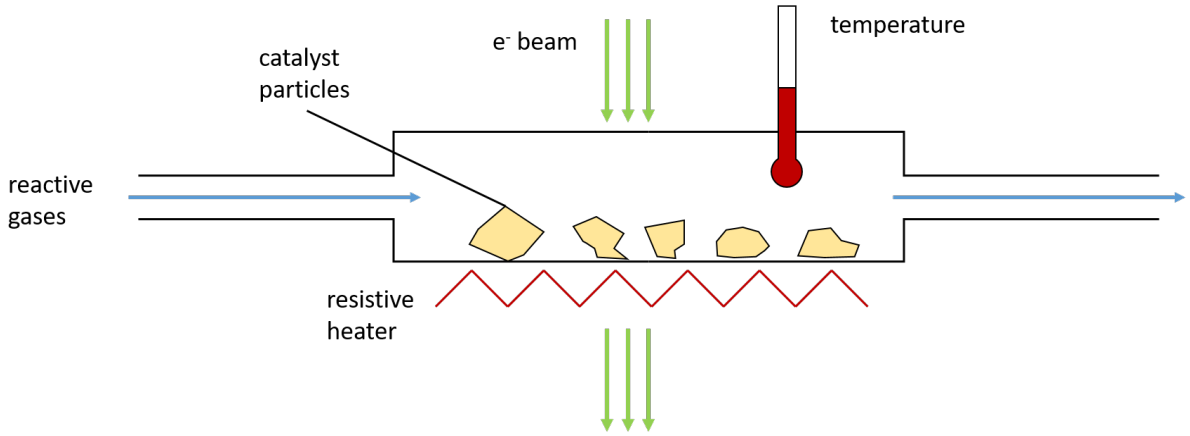

Figure 4.1: The closed nanoreactor concept for operando TEM. Adapted from Creemer *et al.* (2011).

Figure 4.1 illustrates the concept of the nanoreactor. Importantly, the heating is done from the outside of the reactor so that the gases cannot react with the heater. Electron transparent

windows need to be present on the nanoreactor so that electrons can pass through but reactive gases are contained. A more realistic view of the nanoreactor is shown in the following figure:

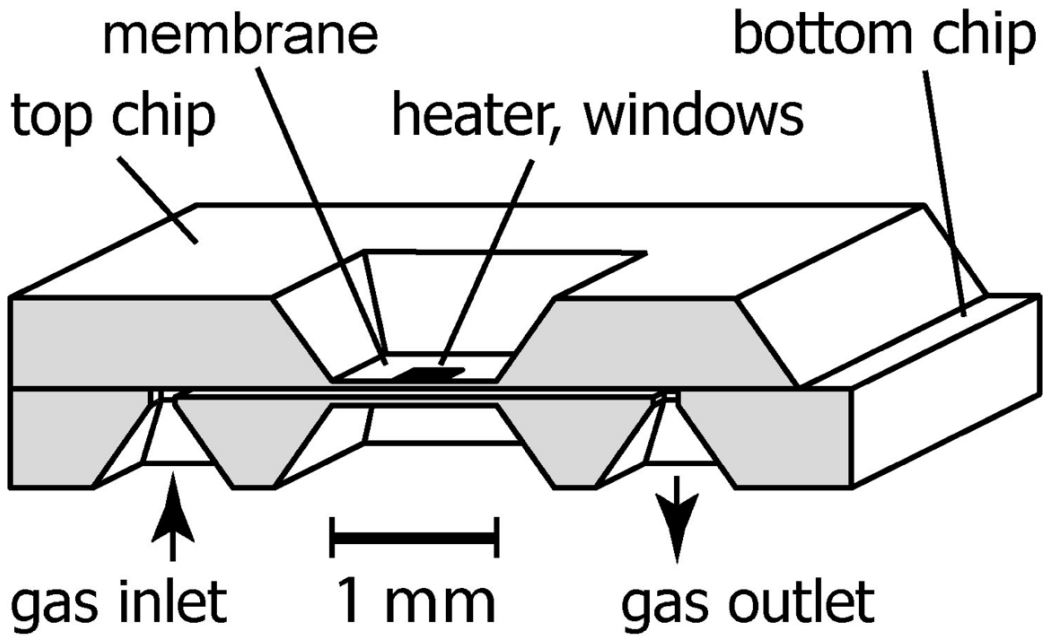

Figure 4.2: A MEMS nanoreactor (Creemer *et al.*, 2008).

A microelectromechanical systems (MEMS) reactor is used to create a nanoreactor that can be inserted into a TEM. It is small enough that it can fit within the same dimensions as a standard TEM holder. In order to load this nanoreactor, catalyst particles are loaded onto the top chip as it is in direct contact with the heater.

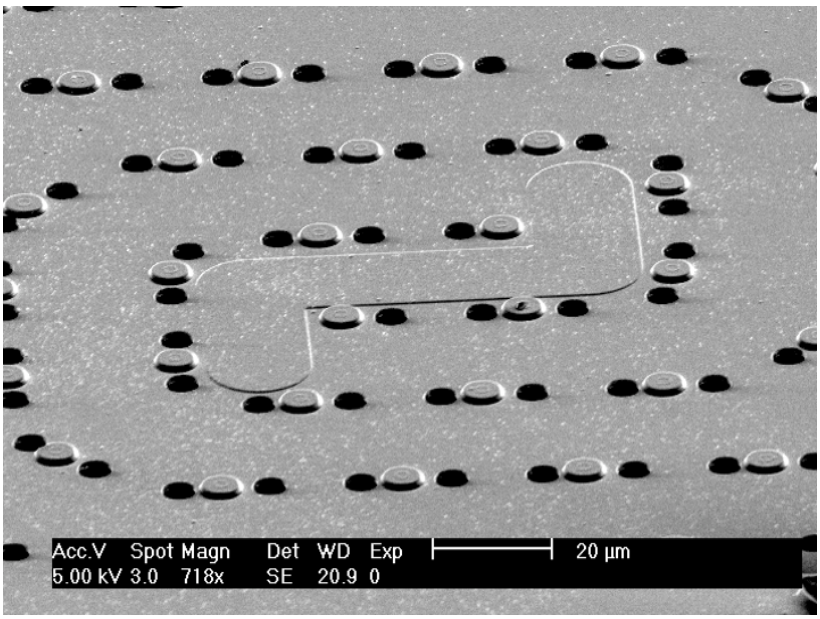

Figure 4.3: SEM micrograph of a MEMS nanoreactor membrane (Creemer *et al.*, 2008).

Figure 4.3 shows one of the nanoreactor's membranes. The bumps that can be seen are pillars that keep the two membranes separate to ensure gas flow around the catalyst. The dark rounded areas in the image are the electron transparent windows, usually made up of silicon

nitride.

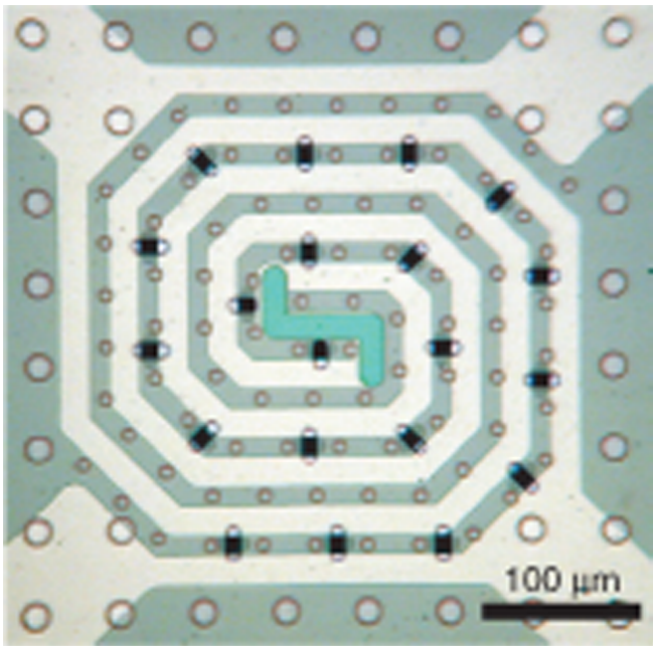

Figure 4.4: Light microscope image of a MEMS nanoreactor (Creemer *et al.*, 2008)

Figure 4.4 is a light microscope image of the nanoreactor, showing the platinum heating spiral. The circles are the pillars, and the dark areas are the electron transparent windows, which are also light transparent. The catalyst would be loaded everywhere, but only heated across this heating spiral to provide temperature control.

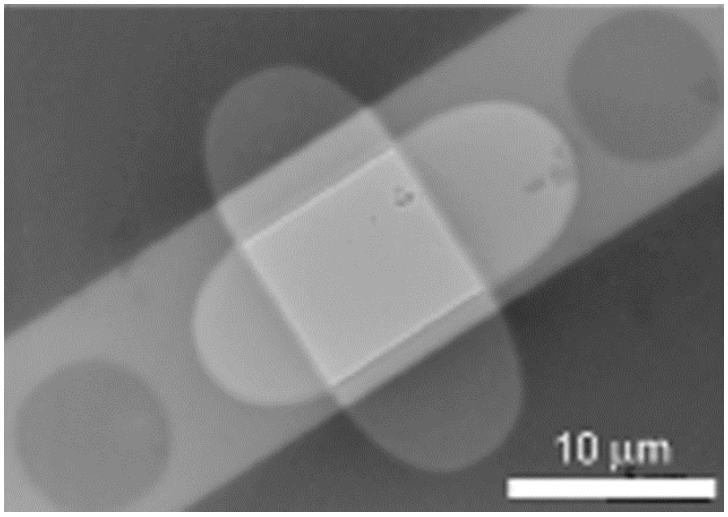

Figure 4.5: TEM micrograph showing the MEMS nanoreactor's overlapping electron transparent windows (Creemer *et al.*, 2008)

From figure 4.5, the importance of overlapping alignment of the windows is exemplified. In the square overlapping zone of the windows, some catalyst particles can be seen, which are more in focus than the particles that are seen through only one window (to the right of the square zone). It is therefore important that the loading of the nanoreactor is sufficient for cata-

lysts to be present in the zones of overlap, but not obstruct the windows, and that the windows align to allow electron transmission.

The catalysts can be characterised through imaging with the TEM as the reaction progresses, showing changes in catalyst structure. If a residual gas analyser (i.e. a mass spectrometer) is attached to the outlet line of the nanoreactor, the composition of the outlet can be tracked simultaneously. This allows for relations to be drawn between the gas composition and structure of the catalyst, providing insight into its behaviour during reaction.

For the *operando* TEM work, a JEOL JEM-2100 microscope was used. Two temperatures were used, 320 and 350 °C, and a gas composition that is the same as the one given in section 4.4.7. A Protochips Atmosphere system was used for the nanoreactor. The Atmosphere system had been modified to accept water vapour within its inlet and exit lines, by lowering the total working pressures such that water vapour would not condense. Water condensing in the lines, which are not heated, would cause dead volume within the nanoreactor and therefore inhomogeneity. The total pressure in the nanoreactor used was 42 Torr (5.6 kPa) to allow the water present to remain a vapour in the inlet and outlet lines. The residual gas analyser (RGA) attached to the outlet of the nanoreactor interfered with the imaging during operation, so simultaneous acquisition of the gas composition and image could not be done.

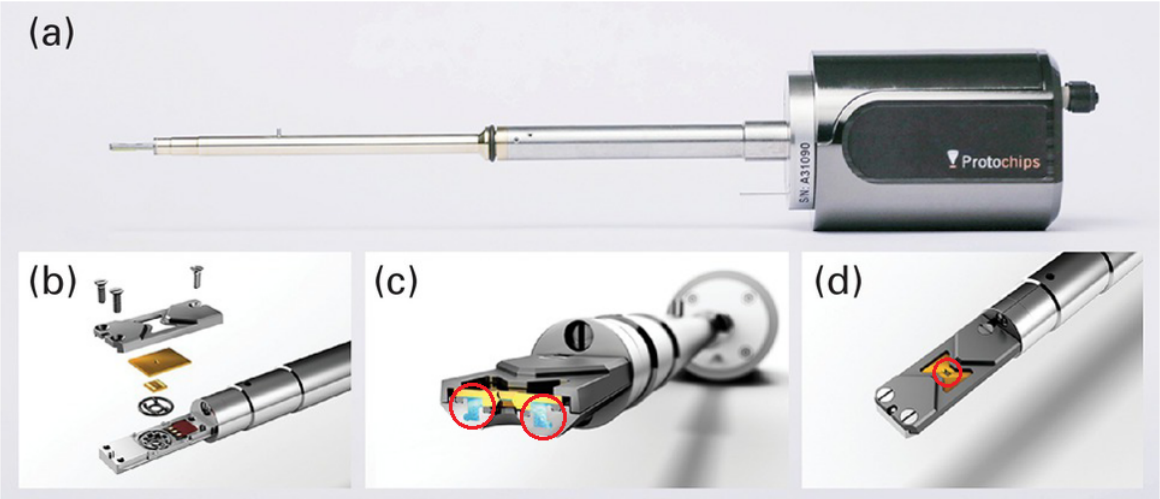

Figure 4.6: Protochips Atmosphere system holder, (a) Overview of the entire holder, (b) detailed view of the tip showing the assembly of the nanoreactor, (c) cross-section showing the gas channels (red circles), (d) the assembled nanoreactor, electron transparent window highlighted (red circle) (Jensen & Mølhave, 2016)

Figure 4.6 shows the Protochips Atmosphere holder that was used. The main difference is shown in the detailed view (b), where the reactor has two chips, with the catalyst loaded onto one chip and then enclosed, whereas the nanoreactor used in Creemer *et al.* (2008) has the catalyst loaded via the gas channel.

4.3.5 Inductively Coupled Plasma Optical Emission Spectroscopy

Inductively Coupled Plasma Optical Emission Spectroscopy (ICP-OES) was used to determine the actual loadings of the platinum and rhenium on the ceria support. ICP-OES uses the characteristic emission spectra of elements excited by plasma to identify and quantify elements present. The analysis was carried out at the UCT Department of Chemical Engineering Analytical Laboratory, using a Varian 730 ES ICP - Optical Emission Spectrophotometer loaded

with Spectra ICP 730 software. The samples were digested with a Mars 6 Microwave digester under the following conditions: 7 mL of 65% HNO_3 and 3 mL of 32% HCl, with ramp and hold times of 30 min each, and a final temperature of 220 °C.

Table 4.3: Sample masses used in ICP-OES analysis

Sample	Mass (mg)
Pt/CeO_2	99
Pt-Re/CeO_2 synthesised by SPS	100
Pt-Re/CeO_2 synthesised by IWI	96

The digested samples (cf. table 4.3 for sample mass) were transferred to a volumetric flask and diluted to 50 mL using 2 wt % HNO_3. The samples were then filtered and analysed. For the analysis of platinum, six multi-element standards were used, and for rhenium, six single element standard were used for calibration with the following concentrations: 0.1, 0.2, 0.5, 1, 2, and 5 ppm.

4.4 Performance Evaluation

The activity and stability of the catalysts were evaluated for the water gas shift reaction using two different temperatures, 320 & 350 °C, and the same gas composition.

4.4.1 Apparatus

The reactor rig has three identical reactors for parallel testing. The reactors have the same inlet composition and temperature, but can have different total reactant feed rates. The reactors are operated vertically, with the gas and water inlets above the outlets. A process flow diagram (PFD) of the rig is shown in figure 4.7.

The gases from the in-house lines are mixed to the desired dry gas composition by the use of the initial mass flow controllers (MFCs). This mixture is backpressure regulated to have a total pressure of 10 bar. Any excess mixed gas is vented to maintain the pressure. The dry gas mixture is then fed to three MFCs, which control the rate of dry gas fed to each reactor. Liquid water is pumped into each reactor at the top, where it vapourises within the reactor.

The reactors are 3/4 inch (internal diameter) packed bed reactors. The reactors are held upright within a heating block that maintains the reaction temperature, and have a thermowell in the middle of each to monitor the reactor temperature. The reactors have the ability to be backpressure regulated, but this was not utilised for this investigation.

The reactor effluent is cooled using a chiller operating at 2 °C to condense water out of the effluent gas. The condensed water is collected in a catch pot that was emptied daily to ensure no water is present in the outlet lines.

The dry reactor effluent gas and the inlet gas are flowed to a 4-way VICI valve. The VICI valve allows each reactor and the inlet gas to be individually sampled using online gas chromatography (GC). When the rig was left running overnight, the valve was set to let all the reactor effluent gases go to vent, to ensure that no water would enter the GC system if the water catch pots overfilled.

GC analysis was carried out using a four column Agilent 490 Micro GC that sampled the dry inlet gas composition and effluent gases. The columns used were a 10 m and 20 m MS5A, and a 10 m PPQ column, while the fourth column was inoperable at the time. The MS5A columns were operated at a pressure of 300 kPa and a temperature of 80 °C. The PPQ column was operated at a pressure of 150 kPa and a temperature of 60 °C. Each column had a heated injector which was operated at 80 °C, with an injection time of 80 μs. The columns were operated in parallel. Galaxie Chromatography software was used for peak identification and integration. See figure A.2 in appendix A.2 for an example of the typical chromatogram produced from the dry reactor outlet gases.

4.4.2 Process Flow Diagram

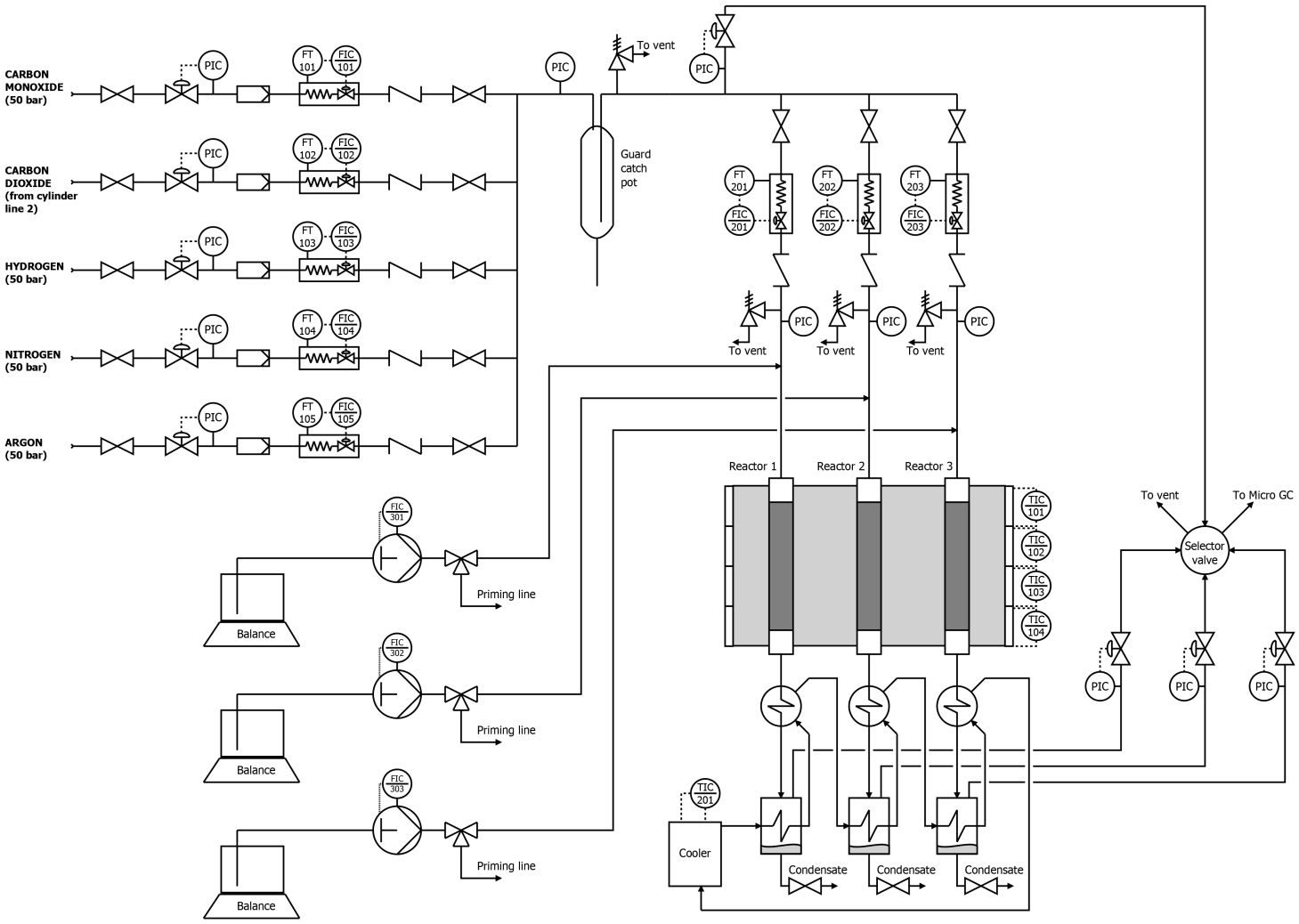

Figure 4.7: Process flow diagram of catalytic performance evaluation set-up (Kruger, 2019)

4.4.3 Calibration

The MFCs were calibrated using a bubble meter and a range of set points, see appendix for details. The flows were all calibrated to STP values. Assessment of the water pumps' flow rate and heater temperature control was done by packing the reactors with inert silicon carbide and flowing nitrogen, as the rig had been previously used and calibration data was available to compare against. These values were found to still be accurate. To find the isothermal zone for each reactor, the temperature was measured along the length of the reactor and found to be at least 10 cm from the bottom of each reactor, extending 15 cm upwards.

4.4.4 Reactor Loading

Each reactor was loaded vertically, using different sizes of inert SiC to pack the tube. First, a wad of glass wool was pushed down to the bottom of the reactor with a metal rod. SiC with an average particle size of 1 mm was loaded until it reached the isothermal zone. Another wad of glass wool was then inserted above this layer. The catalyst was weighed and mixed with approximately the same mass of SiC, having an average particle size of 300 μm. This mixture was then added on top of the glass wool within the isothermal zone. The last wad of glass wool was then inserted on top of the catalyst, with the 1 mm SiC packed on top of this glass wool until it filled the reactor. The reactor was then sealed, inserted into the heating block, and had the gas and water inlets and outlet connected.

4.4.5 Catalyst Pre-Treatment

The catalysts had only been calcined and needed a reduction step. The reduction was carried out in-situ at 350 °C for 8 hours to ensure full reduction, based on the work done by Del Villar *et al.* (2016). The temperature was ramped at 1 °C/min. The reducing gas was 15 % hydrogen in nitrogen, with a flow rate of 150 mL/min (STP) to each reactor.

4.4.6 Analysis of Gas Chromatography Data

Four different mixtures of hydrogen, nitrogen, carbon monoxide and carbon dioxide were used to calibrate the GC and determine the relationship between peak area and gas concentration (refer to table A.4 in appendix A.2 for mixture details). For calculation of the conversion of carbon monoxide, a mass balance had to be performed over the reactor as the lack of water in the dry effluent gas needed to be accounted for. The equation used to calculate conversion was (Kruger, 2019):

$$X_{CO} = \frac{1 - \frac{y_{CO}}{y^0_{CO}}}{1 + y_{CO}} \tag{4.2}$$

Where:

- X_{CO} is the conversion of carbon monoxide
- y_{CO} is the carbon monoxide fraction in the dry reactor effluent gas
- y^0_{CO} is the carbon monoxide fraction in the dry reactor inlet gas

4.4.7 Evaluation Conditions

The gas composition used for all performance evaluation (including the *operando* work) was: 5 % CO, 10 % CO_2, 33 % H_2O, 30 % H_2, 22 % N_2. This composition was based on the work of Radhakrishnan *et al.* (2006), who gave it as the outlet composition of a high temperature steam reformer. The temperature of this reformate stream was 320 °C, which was also one of the temperatures the catalysts were evaluated at. The catalysts were also evaluated at 350 °C, in order to match the temperature they were exposed to in the *operando* work. The space velocity for each catalyst was 32000 $mL/g_{catalyst}/hr$, which ensured that all catalysts had a conversion below 100 % to enable comparison of their activities. The gas flow rate was normalised to the total mass of catalyst and not Pt metal mass as at the time of performance evaluation the actual loading was not known, so the nominal loading of 1 wt. % metal was assumed.

The catalyst loadings for each reactor are given in the table below:

Table 4.4: Catalyst loadings for each experiment

Run	Temperature (°C)	Pt (g)	Pt-Re IWI (g)	Pt-Re SPS (g)
1	320	0.44650	0.48086	0.45059
2	350	0.43266	0.43129	0.41521

Pt refers to the Pt/CeO_2 catalyst prepared by SPS, Pt-Re IWI refers to the $Pt\text{-}Re/CeO_2$ catalyst prepared by IWI, and Pt-Re SPS refers to the $Pt\text{-}Re/CeO_2$ catalyst prepared by SPS.

Chapter 5

Synthesis and Optimisation of Pt-Re Nanoparticles

A method to synthesise homogeneously alloyed Pt-Re nanoparticles was found in the work of Raciti *et al.* (2016). In this chapter, the method to synthesise Pt_3Re nanoparticles that have an average size of 6 nm (no particle size distribution was published) and a spherical shape was shown. This method was reproduced and the results analysed, with modifications done to reduce the particle size and have a more uniform particle size distribution.

5.1 Reproduction from Literature

For Raciti *et al.* (2016)'s method, the tungsten hexacarbonyl ($W(CO)_6$) is added when the solution containing the platinum and rhenium precursors, solvent and surfactants is at 110 °C. The mixture is then heated to 200 °C and left to age for 30 minutes before being removed from heat and left to cool to ambient temperatures by the surrounding air. This method was followed, and the nanoparticles were analysed for size and shape to see if monodisperse particles had been produced. The nanoparticle shape was also analysed to see if it was uniform, as different shapes can affect catalytic performance, introducing unwanted variance.

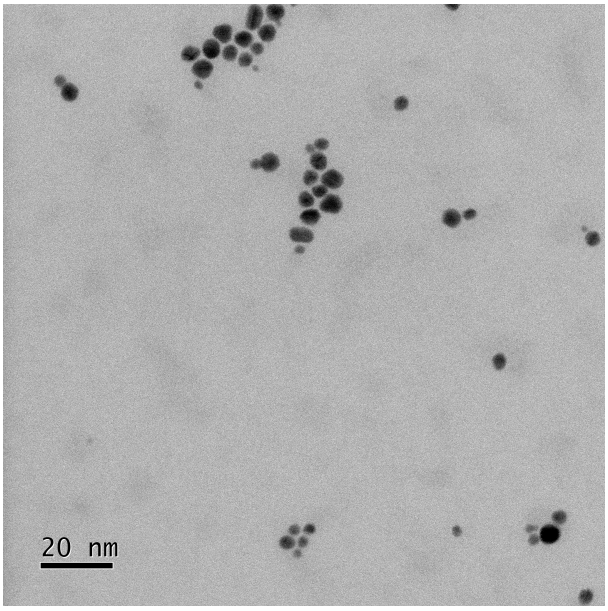

Figure 5.1: TEM image of Pt-Re Nanoparticles synthesised using the method of Raciti *et al.* (2016).

Figure 5.1 shows the nanoparticle's shape and sizes. There are large ($\geq$ 7 nm) and small nanoparticles ($\leq$ 3 nm) present, indicating a polydisperse PSD which is unwanted as larger nanoparticles utilise the precious Pt metal less efficiently due to a higher volume to surface area ratio. In addition, the smaller nanoparticles are more spherical than the larger nanoparticles, which have multiple shapes, including triangular and pentagonal projections. The number of edges, steps, and kinks affects the rate of the reaction on the surface (van Santen, 2009). This number differs for each shape, and so a uniform shape is desired in order to eliminate shape-related effects. A spherical shape is targeted in this synthesis as the nanoparticles synthesised using IWI are also spherical, enabling fair comparison between the two synthesis methods.

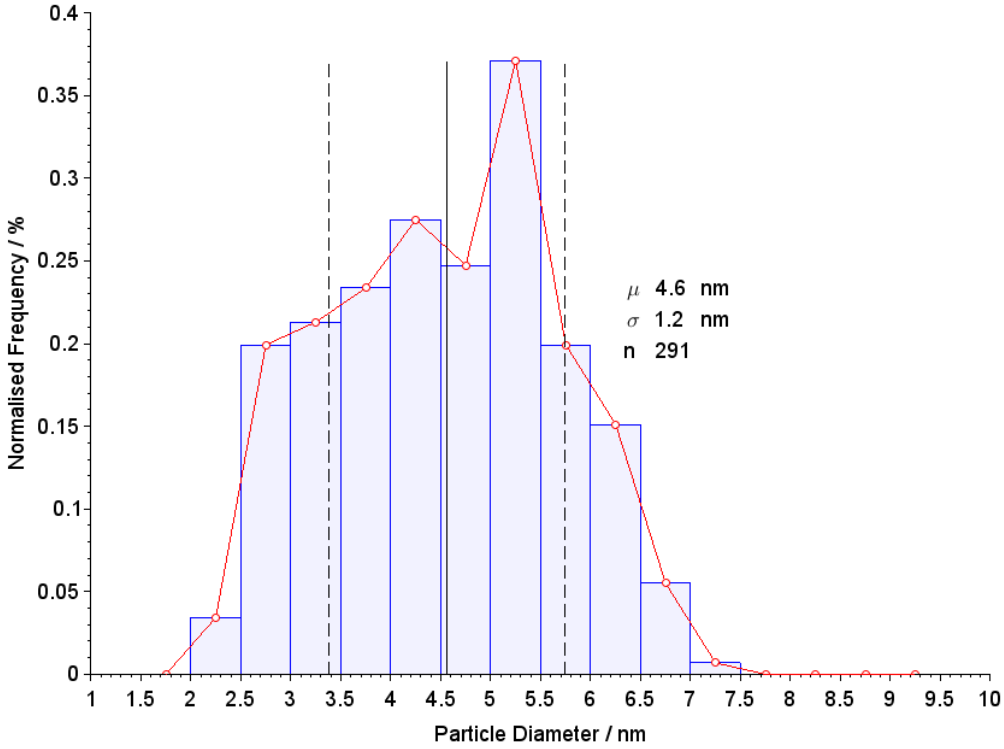

Figure 5.2: Particle size distribution of nanoparticles synthesised from the method of Raciti *et al.* (2016). Frequency polygon shown in red. μ is average, σ is standard deviation, and n is number of particles.

Figure 5.2 shows the histogram of the particle sizes synthesised using Raciti *et al.* (2016)'s method. The average nanoparticle size is 4.6 $\pm$ 1.2 nm, which is smaller than the literature size of 6 nm, but the distribution is very broad. This indicates that particles are not being nucleated in one burst to produce a monodisperse distribution, but are instead nucleated over the entire time the precursor is in solution. Multiple nucleation events could be caused by the $W(CO)_6$ not dissolving and decomposing immediately at 110 °C, which would release the CO unevenly over time. The uneven release of CO would cause the $Pt(acac)_2$ precursor to be reduced unevenly, causing multiple nucleation events. All nanoparticles would grow at similar rates, but due to not nucleating simultaneously they would be at different sizes when the reaction is stopped, thus causing the broad size distribution.

The time taken to reach 200 °C was not specified in the work of Raciti *et al.* (2016). During the heating, the $W(CO)_6$ dissolves and decomposes to release CO, the rate of which is affected by the temperature. As the temperature increases, the rate of dissolution and decomposition of $W(CO)_6$ will increase, leading to a broad particle size distribution. One way to try and prevent this is to keep the mixture at a constant temperature upon addition of $W(CO)_6$ and use ageing time to control particle size.

5.2 Optimisation of the Solution Phase Synthesis Method

The relationship between temperature, ageing time, and particle size was not known for this synthesis method, so a series of syntheses at different temperatures was performed. The temperatures chosen were 120, 140 and 160 °C, and the times for each sample are given in the following table:

Table 5.1: Sampling times used to optimise the SPS method.

Temperature (°C)	**Sampling Time (min)**			
120	30	90	150	N/A
140	15	30	45	60
160	10	20	30	40

The sampling times were chosen such that the intervals between each were shorter as the temperature increased, to account for the increased rate of growth. This optimisation was performed to determine the conditions for producing the smallest and most spherical nanoparticles, with the expectation that a short ageing time and high temperature would achieve this. Sampling after a longer ageing time was expected to show larger particle sizes, so only enough samples were taken to produce a trend and reduce analysis time.

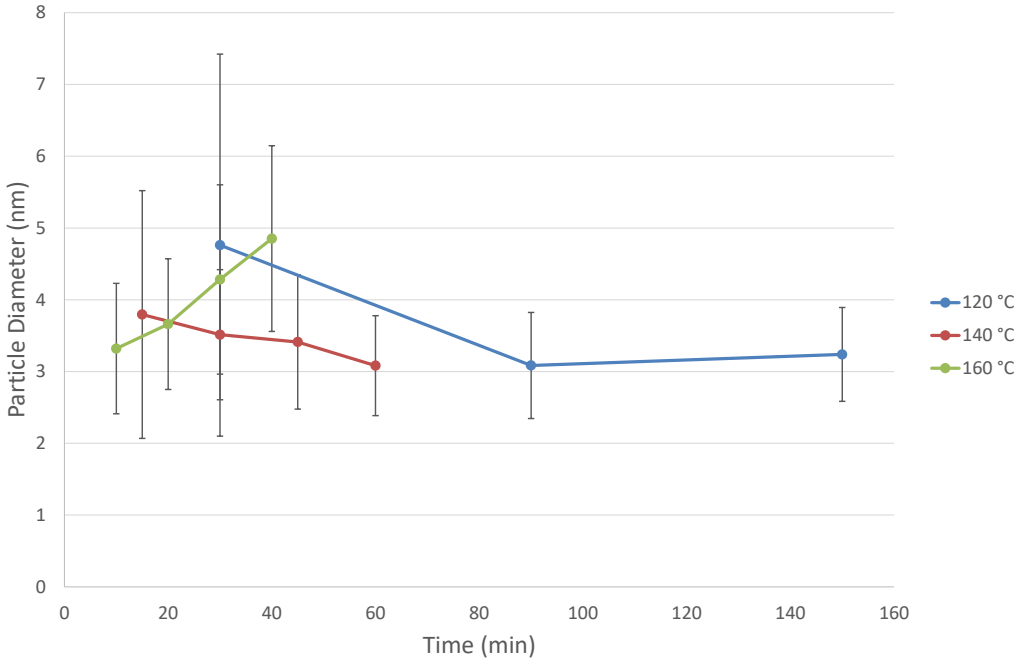

Figure 5.3: Average particle size of Pt-Re nanoparticles as a function of temperature and ageing time.

Figure 5.3 shows the results of the optimisation procedure. The particle size distributions for each plot point is given in appendix B. It is not clear why the average particle size should decrease as ageing time increases for the 120 & 140 °C syntheses, as new material should deposit onto the nanoparticles. The 160 °C did show the expected increase in particle size with ageing time. Repetition of all syntheses is required to determine if this was a once-off event or not. Analysis of the reaction mixture at each interval by ICP-OES would also help to determine the cause of this trend.

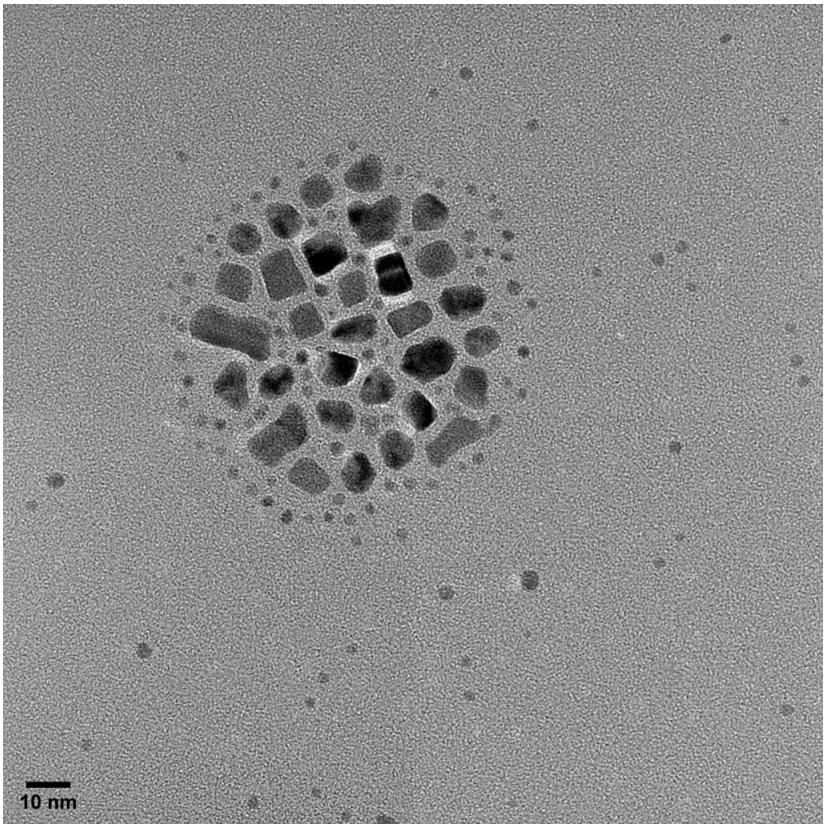

Figure 5.4: TEM image of Pt-Re nanoparticles aged for 30 minutes at 120 °C.

Figure 5.4 shows the Pt-Re nanoparticles after ageing for 30 minutes at 120 °C. It is apparent that the shape is not uniform and the size has a large variance. The large cubic (among other shapes) nanoparticles present among the much smaller spherical nanoparticles shows that a polydisperse distribution had been made. It is unlikely that the small nanoparticles would be able to grow to match the larger nanoparticles during ageing, as surfactants prevent coalescence. Therefore, 120 °C is not a suitable temperature for this synthesis.

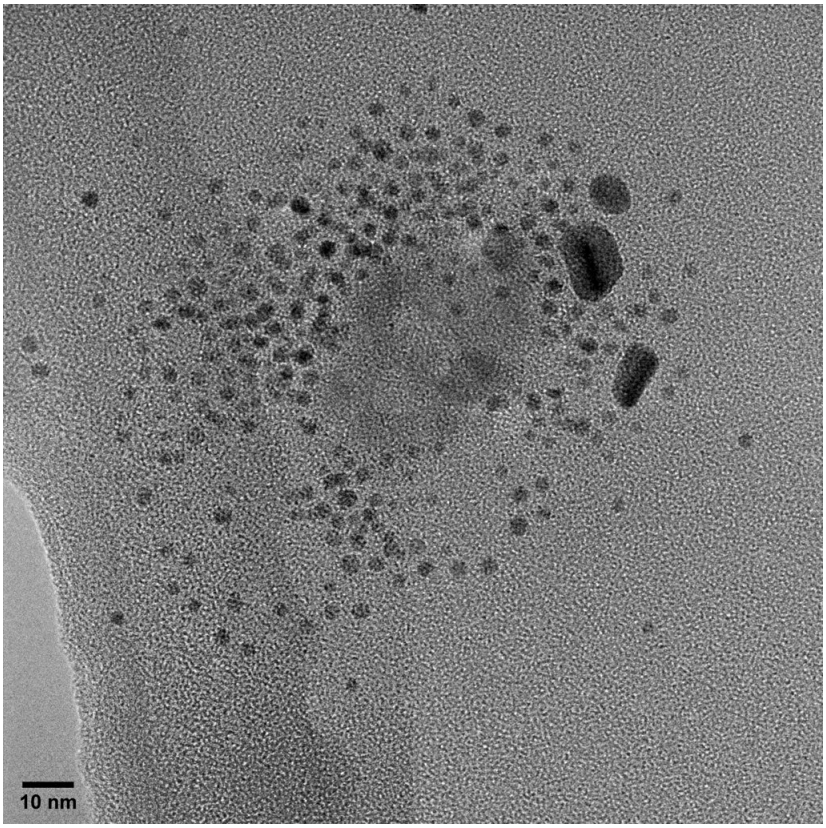

Figure 5.5: TEM image of Pt-Re nanoparticles aged for 15 minutes at 140 °C.

A similar, polydisperse PSD is present for the synthesis at 140 °C, as seen in figure 5.5. Here, the larger, non-spherical nanoparticles are not as large as the ones in the 120 °C synthesis, and have more rounded corners. This indicates a faster growth as there is less time for the more ordered growth as seen in the 120 °C case. Faster growth could be due to the increased temperature enhancing the rate of $W(CO)_6$ dissolution, decomposition and subsequent $Pt(acac)_2$ reduction. However it was not able to produce monodispersed nanoparticles.

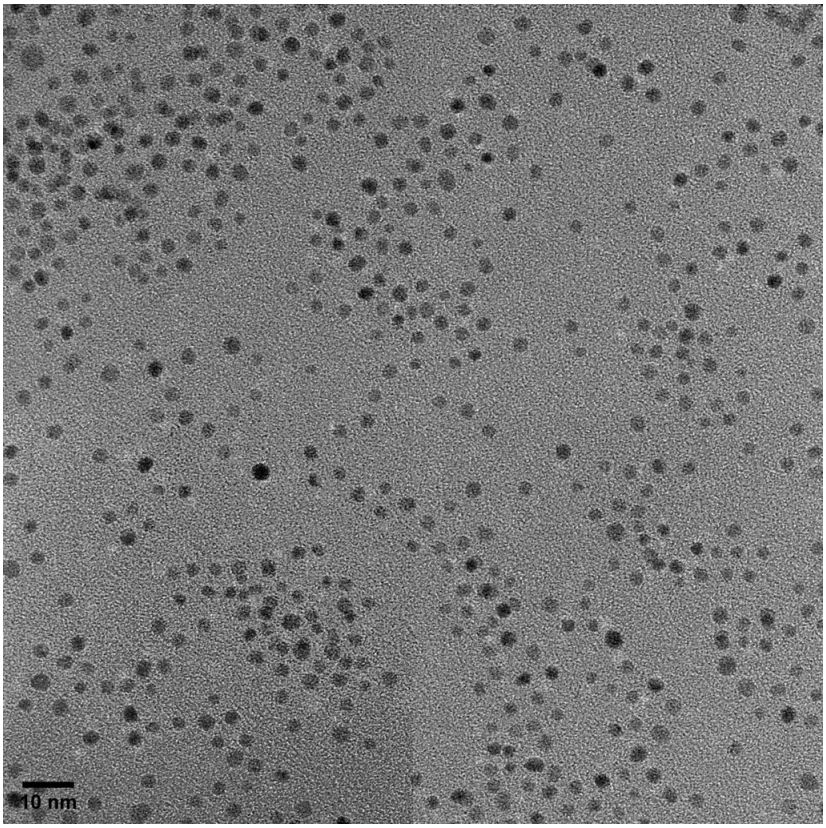

Figure 5.6: TEM image of Pt-Re nanoparticles aged for 10 minutes at 160 °C.

Figure 5.6 shows the nanoparticles synthesised at 160 °C to be monodisperse. This is what was targeted for optimisation of the synthesis method. The temperature is high enough to allow for fast dissolution and reduction of the platinum precursor.

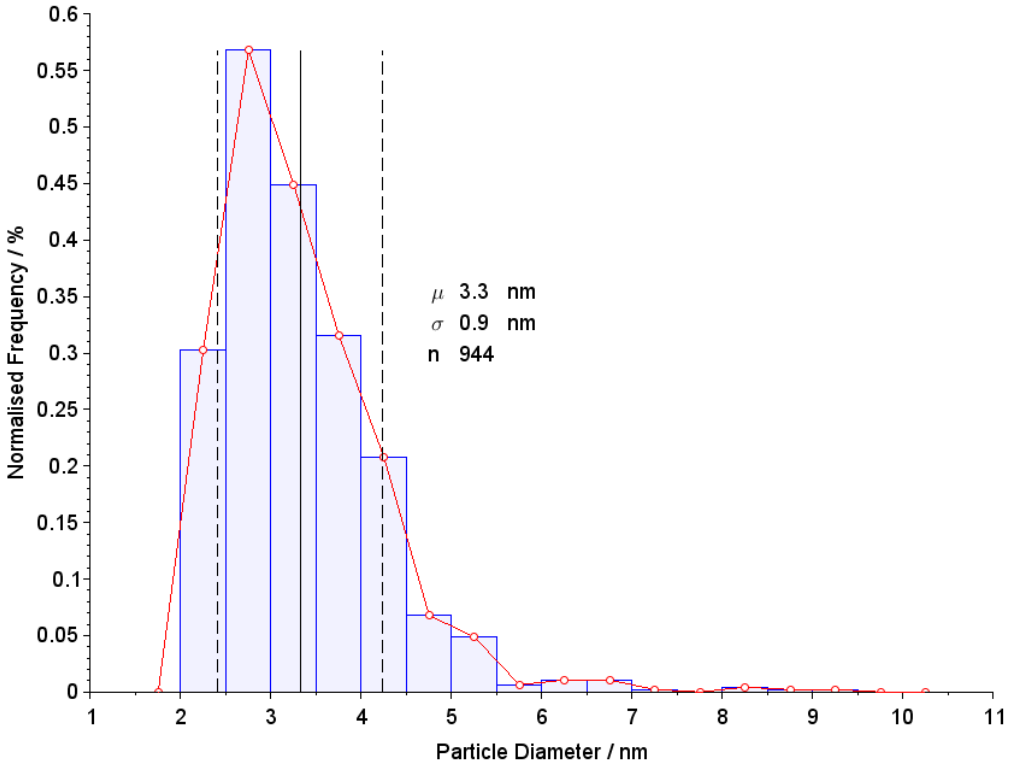

Figure 5.7: PSD of Pt-Re nanoparticles aged for 10 minutes at 160 °C.

The particle size distribution of the nanoparticles, seen in figure 5.7 further confirms monodisperse nanoparticles, with a narrower size distribution and a smaller average particle size (3.3 $\pm$ 0.9 nm) than the method used in replication from literature. The frequency polygon (red line) of the PSD in figure 5.7 indicates that the nanoparticles would best be described by a log-normal distribution. This points to an initial burst of nucleation followed by even growth, with the larger sizes possibly caused by agglomeration. Therefore, ageing the nanoparticles for 10 minutes at 160 °C will be able to produce the small, spherical monodispersed nanoparticles required for the synthesis of a Pt-Re/CeO_2 catalyst via SPS.

Ageing the nanoparticles for 10 minutes at 160 °C most likely is not enough time to produce a high yield of nanoparticles from the reactants, potentially due to incomplete reaction or dissolution (especially of the rhenium precursor). A high yield is important due to the high cost of platinum and the $Pt(acac)_2$ reagent used, especially if trying to scale the catalyst up for pilot or larger reactor systems.

Analysis of the reaction mixture by ICP-OES was not possible due to the presence of organics, and the university's ICP-OES being configured for acid digestion. If the reaction mixture were to be analysed by ICP-OES, the amount of platinum, rhenium and tungsten present in the mixture sampled directly from the synthesis, as well as the supernatant after centrifuging, should be quantified.

Chapter 6

Characterisation of Synthesised Catalysts

The characterisation of the fresh supported catalysts was done using a combination of ICP-OES to determine the metal loading, XRD to detect phases present, and TEM to analyse the catalyst morphology. TEM was also used for the unsupported nanoparticles to determine their shapes and size distribution. For the catalysts synthesised by SPS, a fresh batch was made with an ageing time of 10 min and a temperature of 160 °C, as the original batch synthesised at 160 °C (shown in chapter 5) had been aged for 40 min and so could not be used to create the desired catalyst.

6.1 ICP-OES

All of the catalysts had a nominal metal loading of 1 wt %. The Pt-Re catalysts were prepared with an atomic ratio between Pt and Re of 3:1. ICP-OES was used to verify these loadings and the Pt:Re ratio. The ICP-OES results are presented in the table below:

Table 6.1: ICP-OES results showing the Pt and Re loadings on each catalyst.

Catalyst	Pt (wt %)	Re (wt %)	Metal Loading (wt %)	Pt:Re (atomic)
Pt	0.18	0	0.18	N/A
Pt-Re SPS	0.06	0.01	0.07	9.7:1
Pt-Re IWI	0.62	0.43	1.05	1.7:1

Table 6.1 shows that only the catalyst prepared using IWI had a metal loading close to the targeted 1 wt%, being slightly overloaded at 1.05 %. The catalysts prepared using SPS were significantly under-loaded, and represent a loss in yield (by mass) of 82 % and 93 % for the Pt and Pt-Re catalysts respectively. The loss in yield could be due to the change in the synthesis method from literature, as the shorter ageing time and lower temperature could lead to unreacted $Pt(acac)_2$ and $Re(CO)_{10}$ being present in the suspension. The unreacted $Pt(acac)_2$ and $Re(CO)_{10}$ could be present on the support, but in minimal amounts as the nanoparticles are sonicated onto the support after separation from the reaction mixture by centrifuging.

The Pt and Re ratio was not achieved for any of the syntheses, however the IWI method produced a Pt:Re ratio of 1.7:1 which is closer to the desired ratio of 3:1 than the Pt-Re of 9.7:1 produced by SPS. The high platinum to rhenium ratio in the SPS catalyst suggests that the $Re(CO)_2$ was not completely decomposed and able to alloy with the platinum. In order to increase the Pt:Re to 3:1 long ageing times would be required, however this would lead to in-

creased particle sizes.

The IWI method's Pt:Re ratio of 1.7:1 is also far from the nominal ratio of 3:1. This is most likely caused by experimental error during the transfer of the platinum and rhenium metal salts into the water used to make the impregnation solution. The total amount of metal salts used was very small (48.99 mg total), so any slight variation would have a large effect on the ratios. Simply using more salts to make a larger batch of catalyst might help to correct this, as any small variation would have a reduced effect.

6.2 XRD

Powder XRD should be able to determine what crystalline phases are present in the catalyst. If there is a shift in the diffraction lines from the reference patterns of the pure platinum and rhenium metals then it indicates that alloying could have occurred.

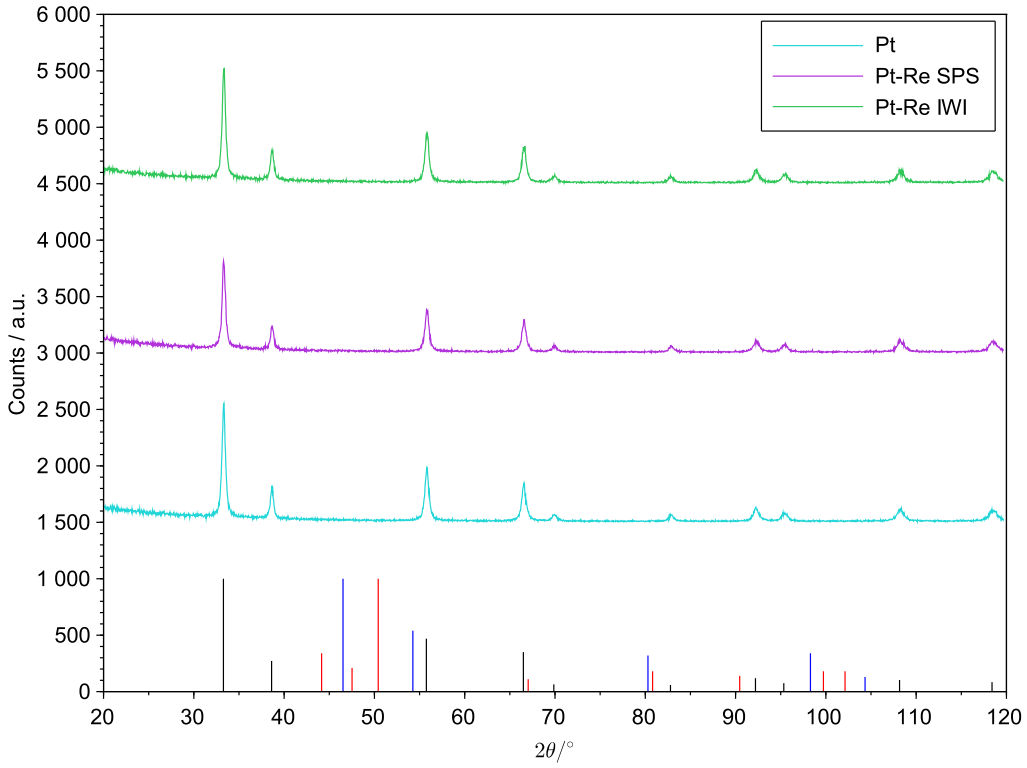

Figure 6.1: Powder XRD of supported catalysts. Reference patterns: CeO_2 - black (PDF 03-065-2975), Re - red (PDF 00-001-1231), Pt - blue (PDF 00-004-0802).

Figure 6.1 shows the result of powder XRD performed on the as-synthesised catalysts. The diffraction lines present in each of the catalyst corresponds to the CeO_2 support. No diffraction lines matched the platinum or rhenium reference patterns, and the strongest reflexes for Pt (46.5°) and Re (50.4°) did not have any diffraction lines shown. The inability of the metal nanoparticles to be detected by powder XRD is likely due to their small sizes (Niemantsverdriet, 2007) (cf. figures 6.3 and 6.5) combined with the low metal loading (1.05% and below) on the support, even with each step taking 6 seconds to eliminate as much noise as possible.

6.3 TEM

TEM was performed on the unsupported Pt and Pt-Re nanoparticles before they were ultrasonicated onto the ceria support. The supported catalysts were also characterised using TEM.

6.3.1 Unsupported Nanoparticles

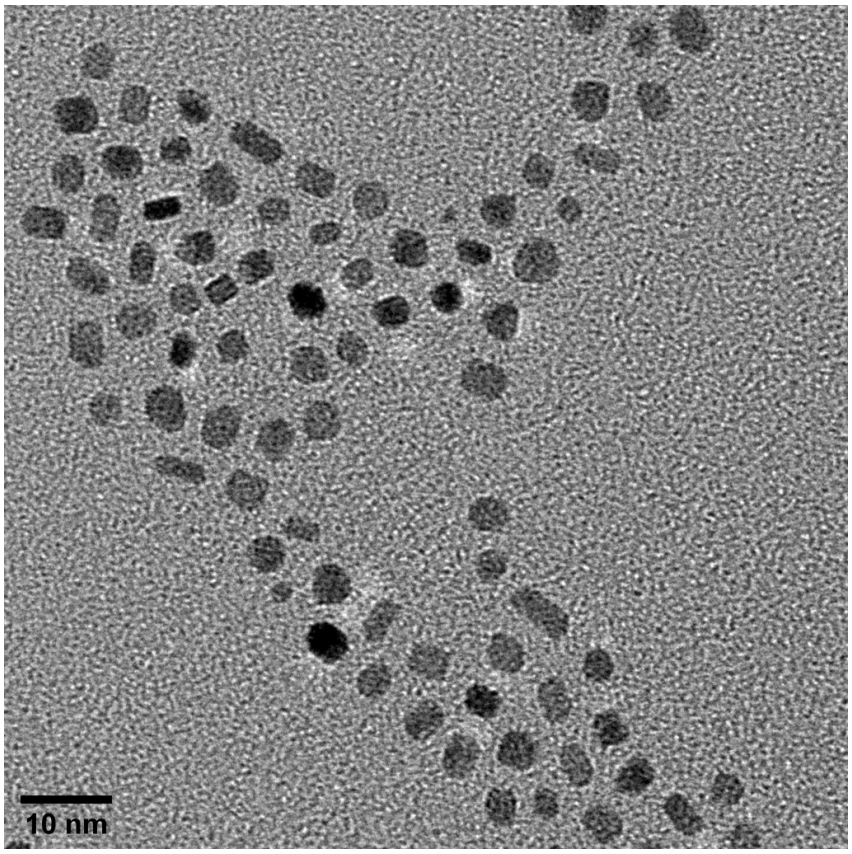

Figure 6.2: Unsupported Pt nanoparticles synthesised using SPS at 160 °C

The unsupported Pt nanoparticles are shown in figure 6.2. These nanoparticles have some non-spherical shapes in them, which could affect the performance of the catalyst during the WGS reaction. The nanoparticles are purely Pt, which could slightly affect their behaviour during SPS synthesis. The synthesis was optimised for Pt-Re nanoparticles, so the absence of Re could have a slight effect on their growth and final shape.

Figure 6.3 shows that the average particle size is 3.8 ± 0.7 nm. The spread is very narrow, and the distribution is close to a normal distribution. The narrow spread also indicates that the targeted monodisperse distribution was achieved.

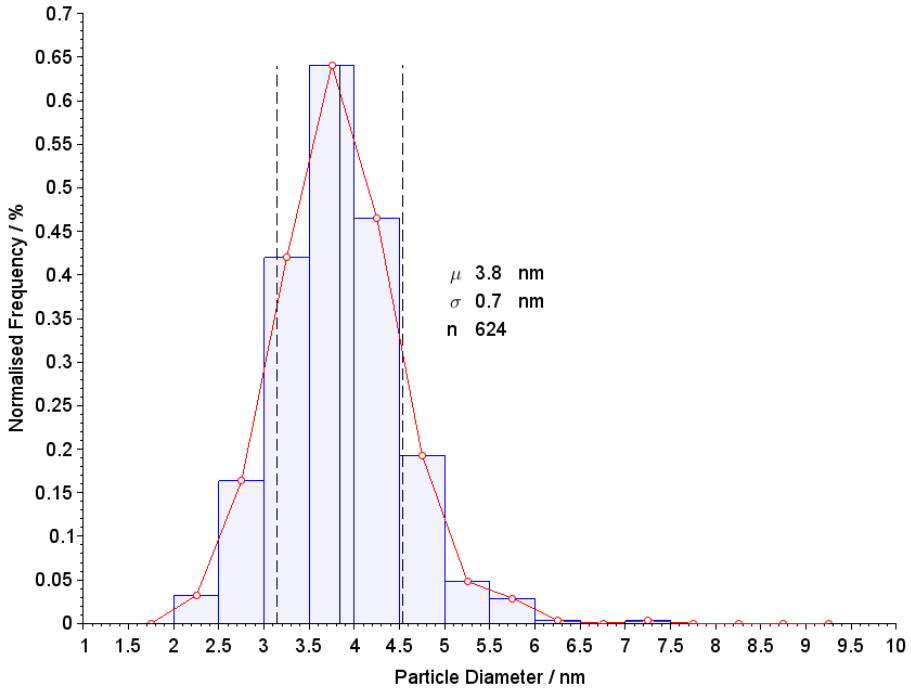

Figure 6.3: PSD of unsupported Pt nanoparticles synthesised at 160 °C

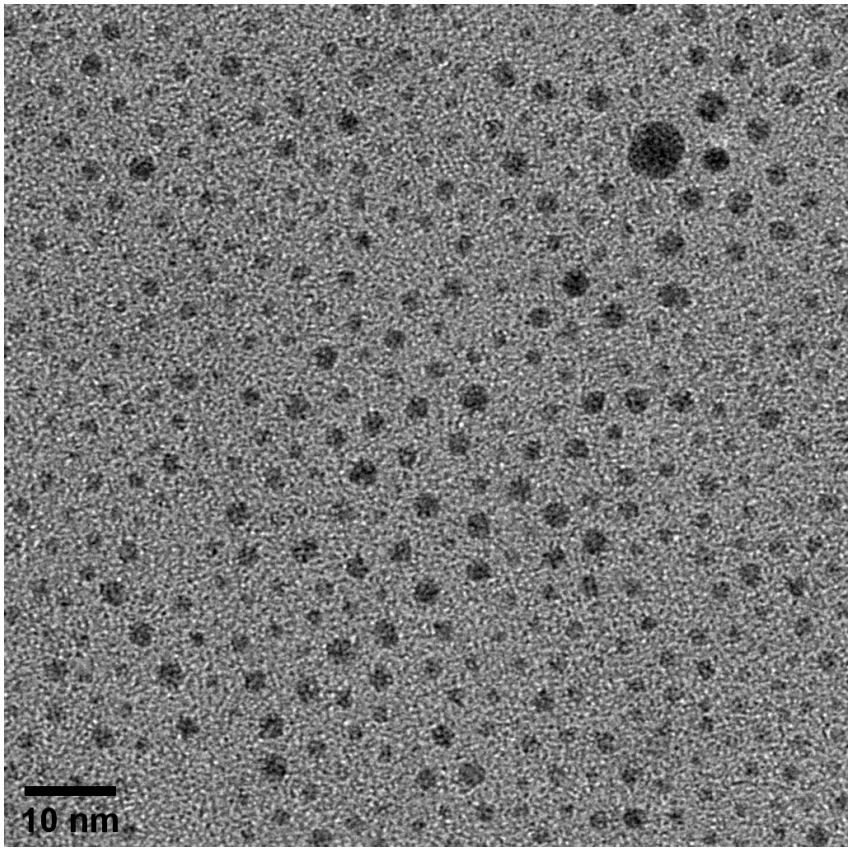

Figure 6.4: Unsupported Pt-Re nanoparticles synthesised at 160 °C

The unsupported Pt-Re nanoparticles are shown in figure 6.4. On average these particles appear to be smaller than the Pt nanoparticles, however their shapes are more spherical. This could be due to the Re present during synthesis affecting the size and shape.

The nanoparticles are also smaller than the nanoparticles in figure 5.6. The expected result is for the nanoparticles to be similar as the same method was used to synthesise both batches. Therefore the method is sensitive to minor changes between syntheses, such as temperature variations during synthesis.

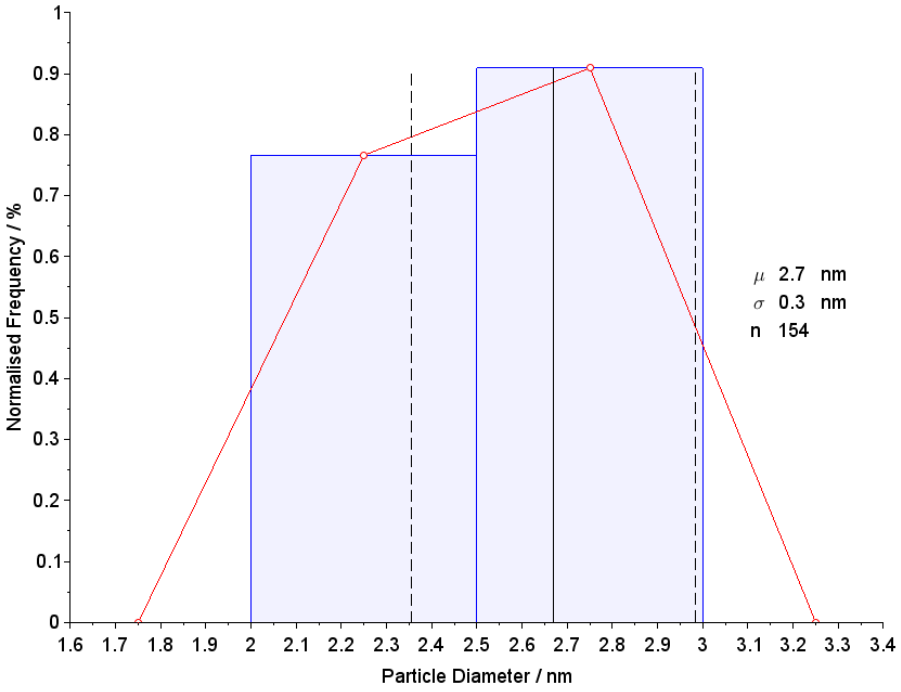

Figure 6.5: PSD of unsupported Pt-Re nanoparticles synthesised at 160 °C

The PSD of the unsupported Pt-Re nanoparticles, shown in figure 6.5, indicates that the average particle size is 2.7 $\pm$ 0.3 nm. This is smaller than the Pt nanoparticle size of 3.8 nm, which may be due to the presence of rhenium. The average particle size range of 3.3 $\pm$ 0.9 nm shown in figure 5.7 overlaps the average particle size range of this batch. Even though the size ranges overlap, it is not enough to say that the synthesis method is fully reproducible, as the current synthesis produced a smaller, narrower range of nanoparticles. At least one more synthesis using the same conditions should be performed to better judge the reproducibility of the synthesis method.

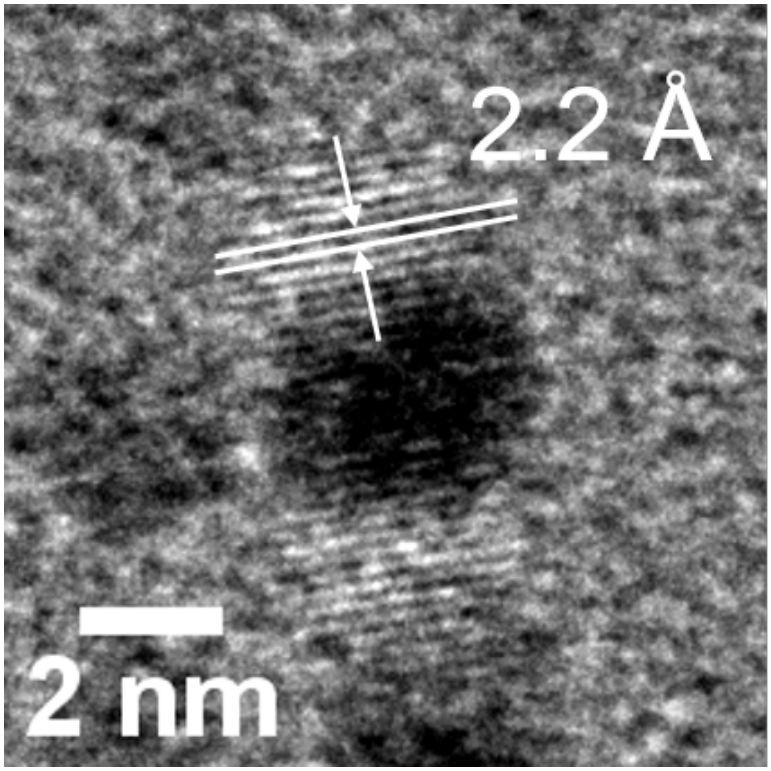

Figure 6.6: High magnification TEM image showing the d-spacing of a Pt-Re nanoparticle

High magnification images were taken of the unsupported Pt-Re nanoparticles to determine the d-spacing. Atomic scale resolution of the nanoparticles was achieved as the lattice fringes can be seen in figure 6.6. The d-spacing of 2.2 Å corresponds to the (111) plane of a face-centred cubic (fcc) crystal of a Pt_3Re nanoparticle (Raciti *et al.*, 2016). A d-spacing of 2.2 Å also corresponds to the Pt (111) crystal plane (PDF 00-004-0802). The (101) crystal plane of rhenium has a d-spacing of 2.1 Å (PDF 00-001-1231), and the accuracy of the d-spacing is not enough to distinguish the small differences between these crystal planes. To confidently say that the nanoparticles are alloyed will require higher accuracy in measurement of the d-spacings.

6.3.2 Supported Catalysts

The Pt/CeO_2 and $Pt\text{-}Re/CeO_2$ (prepared by IWI) that had been calcined, but not reduced, was also analysed using TEM. Reduction is performed in-situ so the reduced catalysts couldn't be characterised before being loaded into the reactor rig.

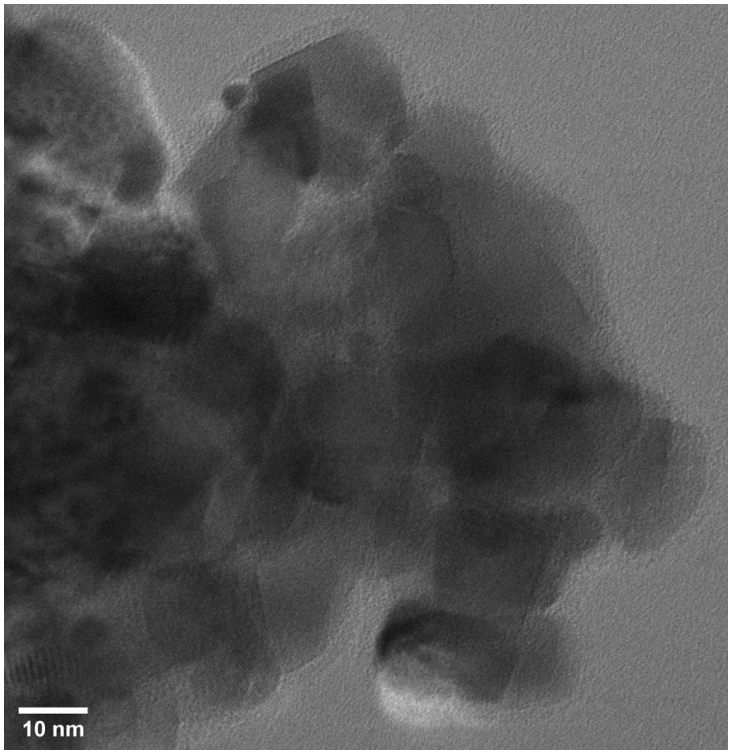

Figure 6.7: Overview of Pt supported on ceria

Figure 6.7 shows the highly crystalline ceria support with some nanoparticles visible, especially nearer the edges and thinner areas. The platinum loading on the support is low, therefore the likelihood of finding and imaging a platinum nanoparticle is subsequently low. Cerium has a Z number of 58, and platinum has a Z number of 78, which decreased contrast in the bright field TEM due to the Z numbers being close to each other.

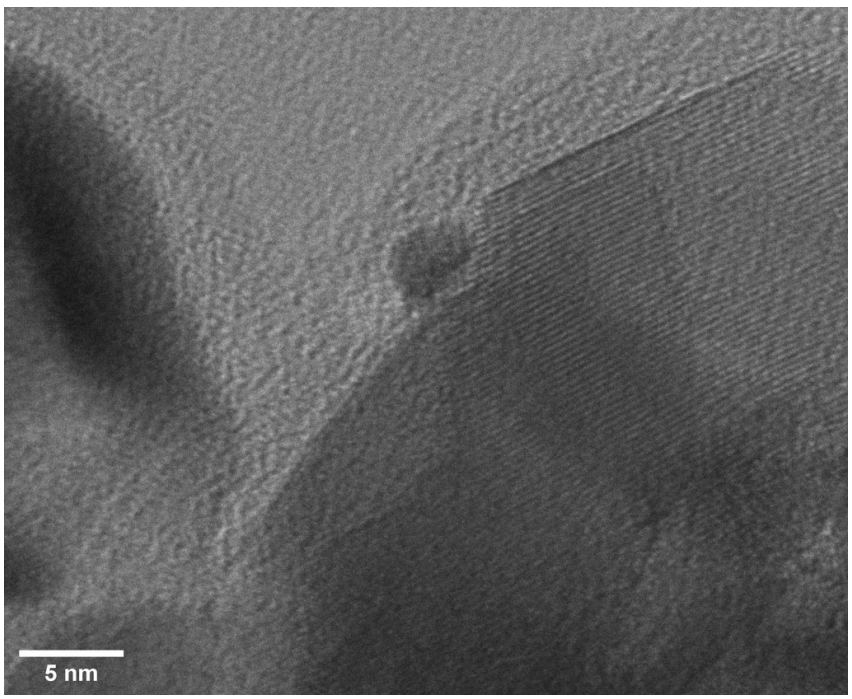

Figure 6.8: Higher magnification TEM image showing a Pt nanoparticle on ceria support.

Figure 6.8 shows a platinum nanoparticle on the edge of the ceria, with a mostly spherical shape. The Pt nanoparticles were synthesised with a spherical shape which has been retained during the calcination step at 190 °C. Therefore, it is likely that the calcination step does not significantly alter the shape of the metallic nanoparticles, due to it being carried out at a low temperature.

The analysis of the Pt-Re nanoparticles prepared by SPS and supported on ceria was not performed as due to the low loading (0.07 wt %) combined with the low contrast, no metal nanoparticles were found on the ceria support. It is unlikely that this would provide new insights as the Pt-Re nanoparticles would be affected the same way during the supporting process due to their similar physical properties to platinum - which is the majority of the nanoparticle content.

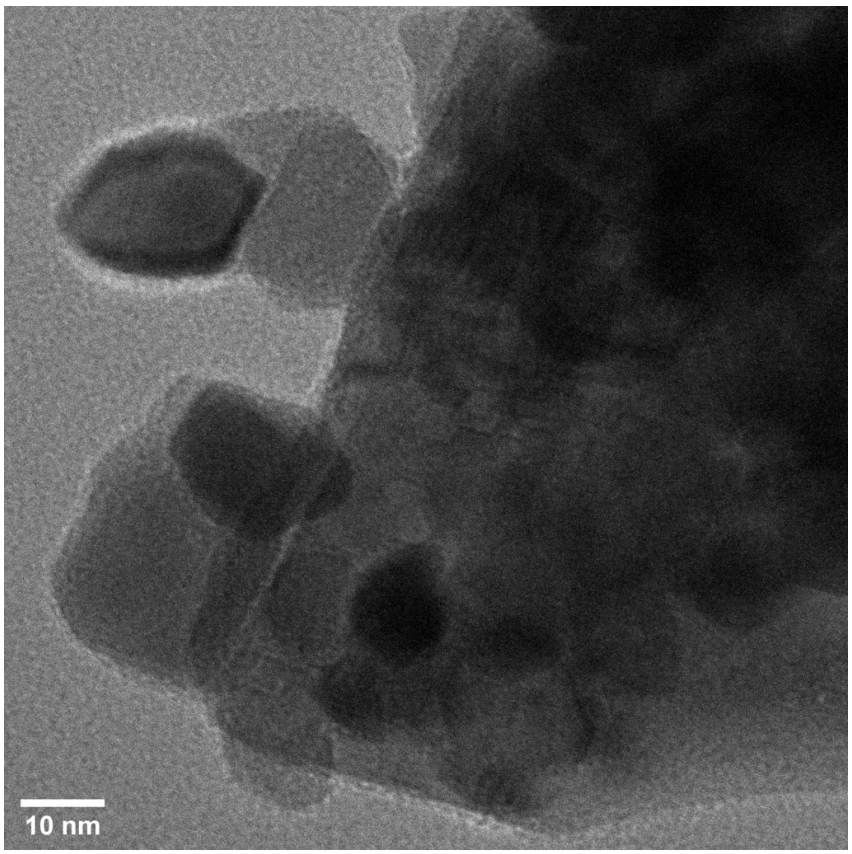

Figure 6.9: The calcined Pt-Re/CeO_2 catalyst prepared by IWI.

The oxidised (but not yet reduced) Pt-Re catalyst prepared by IWI is shown in figure 6.9. The metal oxides were not distinguishable from the ceria support, but are present as the metals are detected by ICP-OES analysis. Bright field TEM was the only microscopy technique available at the time of imaging, limiting analysis. High-angle annular dark field (HAADF) imaging, which produces an image through Z-contrast, is able to pick up the heavier Pt and Re metal oxides and would enable further analysis of the catalyst.

Chapter 7

Operando TEM

Unsupported Pt and Pt-Re nanoparticles were studied using *operando* TEM under water gas shift (WGS) reaction conditions at 320 °C and 350 °C. In all conditions studied, the Pt and Pt-Re nanoparticles changed shape during reaction, morphing between having facets and being spherical. This change is attributed to the gases present, as the gas composition (and any changes thereof) affects the free energy of the exposed surfaces, necessitating a change in shape to minimise energy (Vendelbo *et al.*, 2014; Yoshida *et al.*, 2011). The elevated temperature and the WGS reaction taking place also cause changes in the particles' shape. Observation under WGS reaction conditions indicates that it is likely that this phenomenon happens to the metal nanoparticles at lab or larger scales of reaction.

In all figures presented within this chapter, a white line has been drawn around the border of the nanoparticles to guide the eye.

7.1 Platinum Nanoparticles

The particle was observed for 9 minutes and 41 seconds at 320 °C. During the course of observation,the particle changed between being facetted and spherical. Figure 7.1 shows the difference between these two shapes.

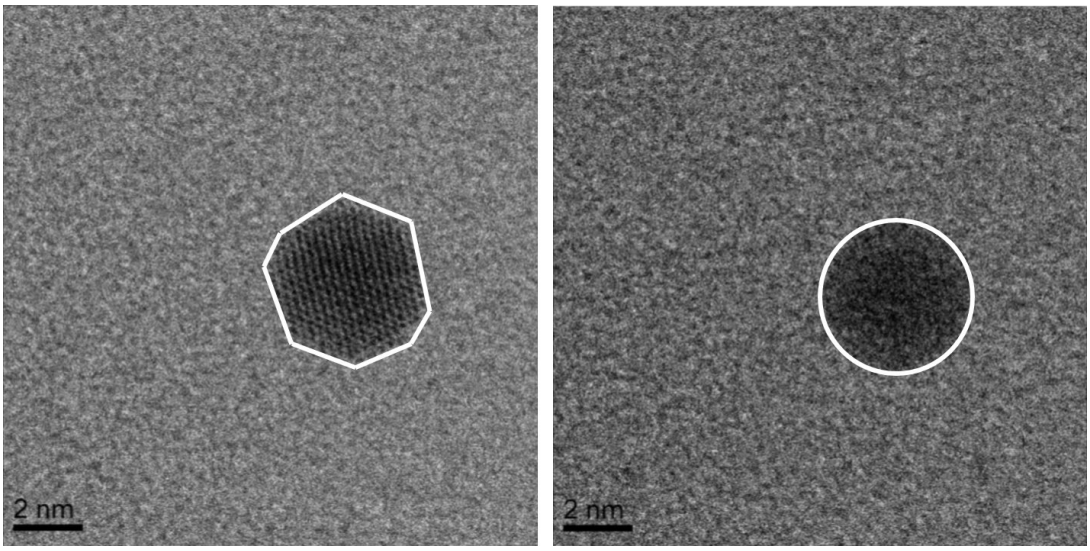

Figure 7.1: Platinum nanoparticle at 320 °C under *operando* WGS conditions. Left: facetted shape. Right: spherical shape.

The particle was also noted to oscillate between being spherical and facetted multiple times during the observation period. Snapshots of this oscillation are shown in figure 7.2, with contours drawn to highlight the difference between the shapes.

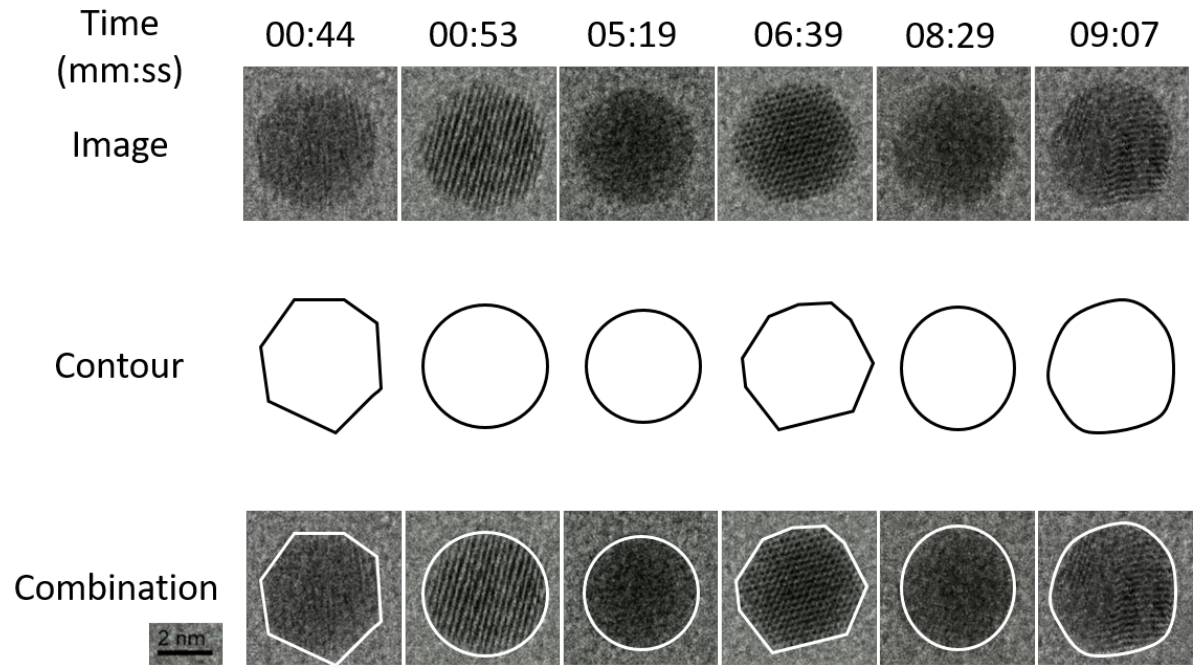

Figure 7.2: Sequence of Pt nanoparticle at 320 °C, sampled from the entire observation period.

The nanoparticle does not return to the same facetted configuration after each transition from a spherical shape. This is shown at the times of 00:44 and 06:39, where the number of edges is different. As this facetted shape is not seen under the vacuum condition of normal TEM operation, it is caused by the gas environment and high temperatures. The gas concentrations also change near the nanoparticle as it catalyses the WGS reaction between the gases adsorbed on its surface. The effects of the gas ratios and the catalysis of the WGS reaction are difficult to separate here in order to explain the difference between the facetted shapes.

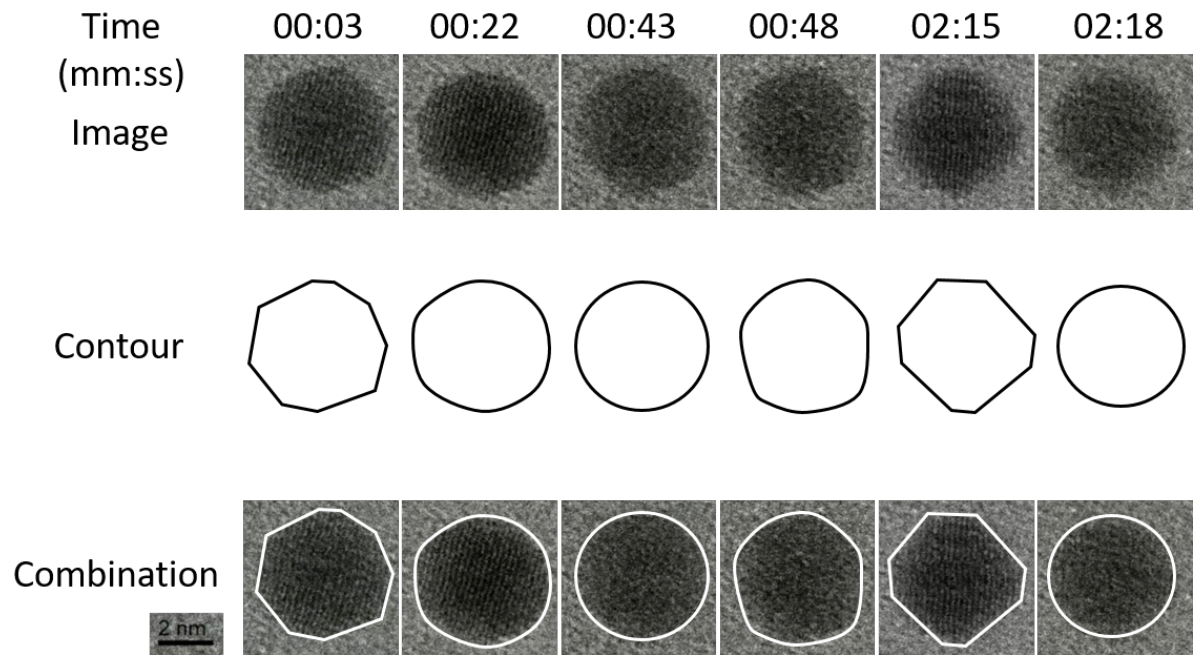

Figure 7.3: Sequence of Pt nanoparticle at 350 °C, sampled from the entire observation period.

The nanoparticles were then heated to 350 °C under the same gas conditions, and observed for 2 minutes and 23 seconds. Figure 7.3 shows the particle oscillating between facetted and spherical as well, in the same manner seen at 320 °C. At the 00:22 and 00:48 timestamps, the particle is in-between facetted and spherical, having sharp and rounded edges.

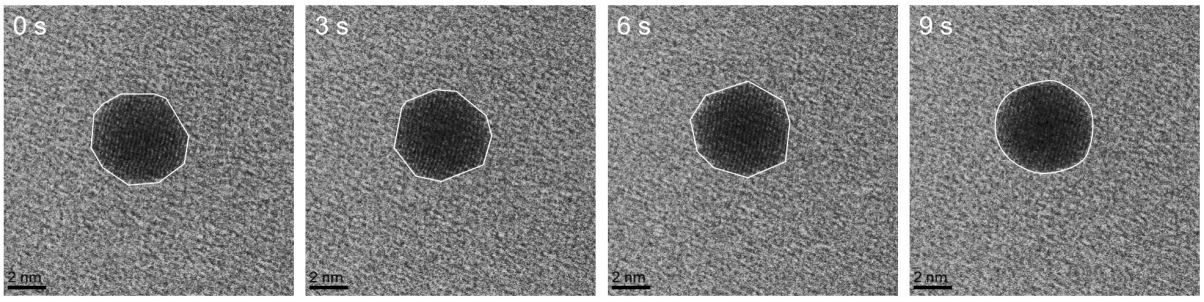

Figure 7.4: Image sequence showing the oscillation behaviour of a Pt nanoparticle at 350 °C under *operando* WGS conditions.

The sequence of images shown in figure 7.4 shows the steps between the facetted and spherical shapes. The nanoparticle is facetted initially at 0 s, and at 3 and 6 s it is still facetted, however the number and locations of the facets has changed between each step. The final image at 9 s shows the nanoparticle in a more spherical shape.

7.2 Platinum-Rhenium Nanoparticles

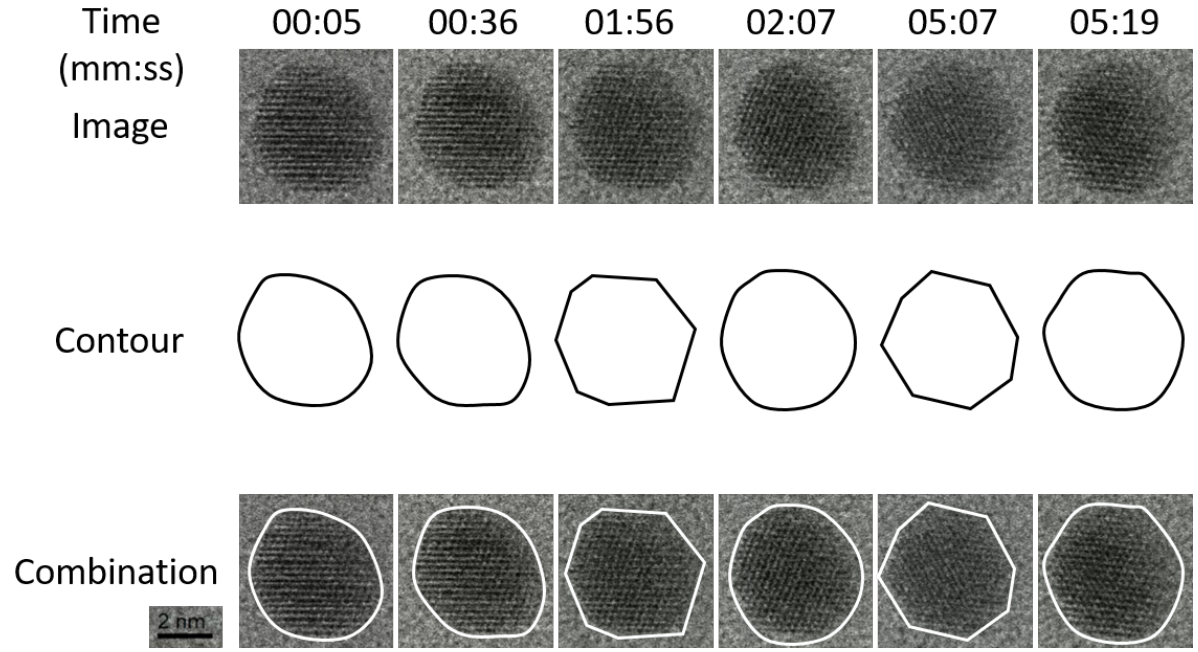

Figure 7.5: Sequence of Pt-Re nanoparticle at 320 °C, sampled from the entire observation period.

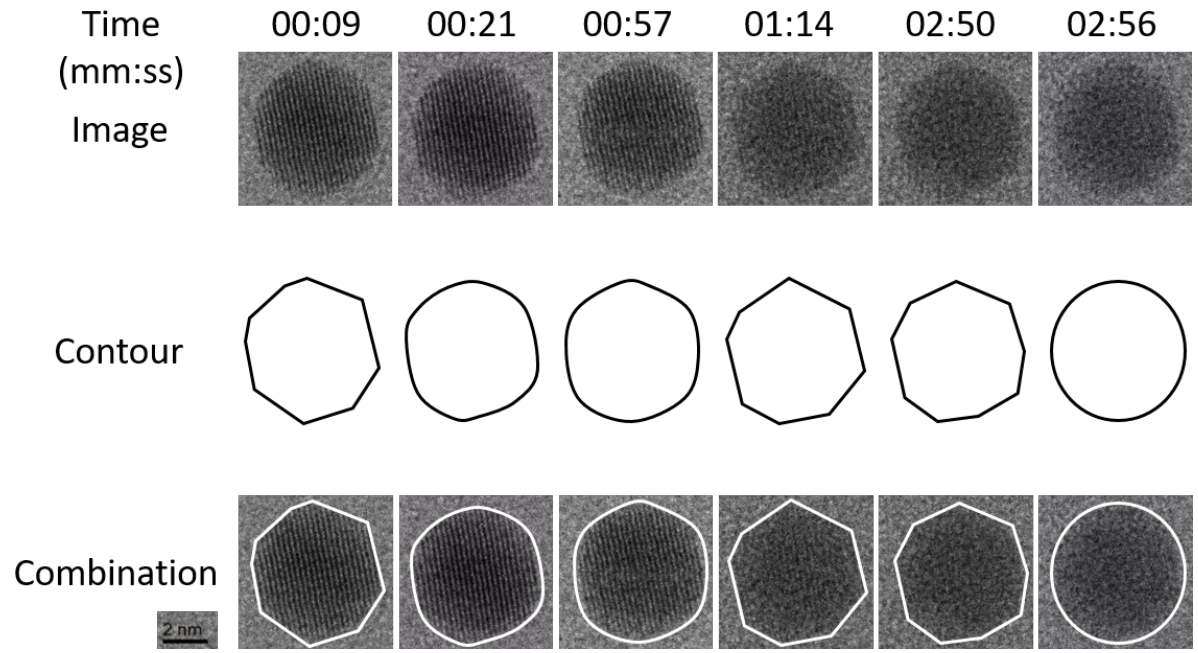

Figure 7.6: Sequence of Pt-Re nanoparticle at 350 °C, sampled from the entire observation period.

The platinum-rhenium nanoparticles exhibited the same behaviour as the platinum nanoparticles - oscillating between spherical and facetted at 320 °C and 350 °C.

The nanoparticle in figure 7.5 was observed for 6 minutes and 16 seconds, and snapshots are shown to demonstrate the spherical and facetted shapes it had. This is similar to what was seen in figure 7.2. After observation at 320 °C, the nanoparticles were also heated to 350 °C. Snapshots of a nanoparticle observed for 3 minutes and 53 seconds are shown in figure 7.6, also showing similar behaviour as observed in figure 7.2.

The similarities in behaviour of the Pt and Pt-Re nanoparticles can not show that the addition of rhenium alters behaviour of the platinum nanoparticles. The overall fraction of rhenium present in this sample is very low, as determined by ICP-OES in table 6.1. Therefore, it is not certain that rhenium is present in these two nanoparticles, and they could be pure platinum . If these particles are purely platinum then the similarity in behaviour is to be expected.

These oscillations are also similar to what was observed by Vendelbo *et al.* (2014), who oxidised CO with O_2 over a platinum catalyst at 450 °C. The pressures used were higher at 1 bar compared to the pressure of 5.6 kPa used in this work, so the oscillations happened more rapidly than the ones shown here. This could mean that at the higher pressures of lab (or greater) scale reactors, which ranges from 1 atmosphere and higher, the oscillations also occur more frequently.

The exact cause for the oscillations under WGS conditions is difficult to determine as the gas environment and temperature is different to that of Vendelbo *et al.* (2014), and there was no RGA available for these experiments to determine the gas composition at the time of the oscillations. In order to try and determine the cause and its effects on the catalysis of the WGS reaction, more experimental data is required. These experiments should vary the concentrations of gases present to determine the effect of each gas on the nanoparticles. Coupling a RGA to the gas outlet would also show whether a reaction takes place during the oscillations. A wider range of temperatures, especially below 320 °C should also be investigated to determine what the onset temperature is for the oscillations.

These nanoparticles were observed without the ceria supporting them. In order to more confidently say that this behaviour occurs at larger scales, the nanoparticles would have to be observed with the ceria support.

Chapter 8

Catalyst Performance Evaluation and Post-Run Characterisation

Lab-scale performance evaluation of the catalyst was done to determine which synthesis method produced the most active and stable WGS reaction catalyst. These evaluations also allowed for an opportunity to run the experiments for a longer duration than what *operando* work allows. For these runs, the catalysts were tested at 320 °C and 350 °C, using fresh catalyst for each temperature.

8.1 Performance Evaluation

The conditions for the ex-situ runs were identical in temperature and gas composition to that used in the *operando* work. The reactor outlet gases were sampled at approximately the same time each day during their runs, along with the inlet to ensure accuracy in the conversion obtained.

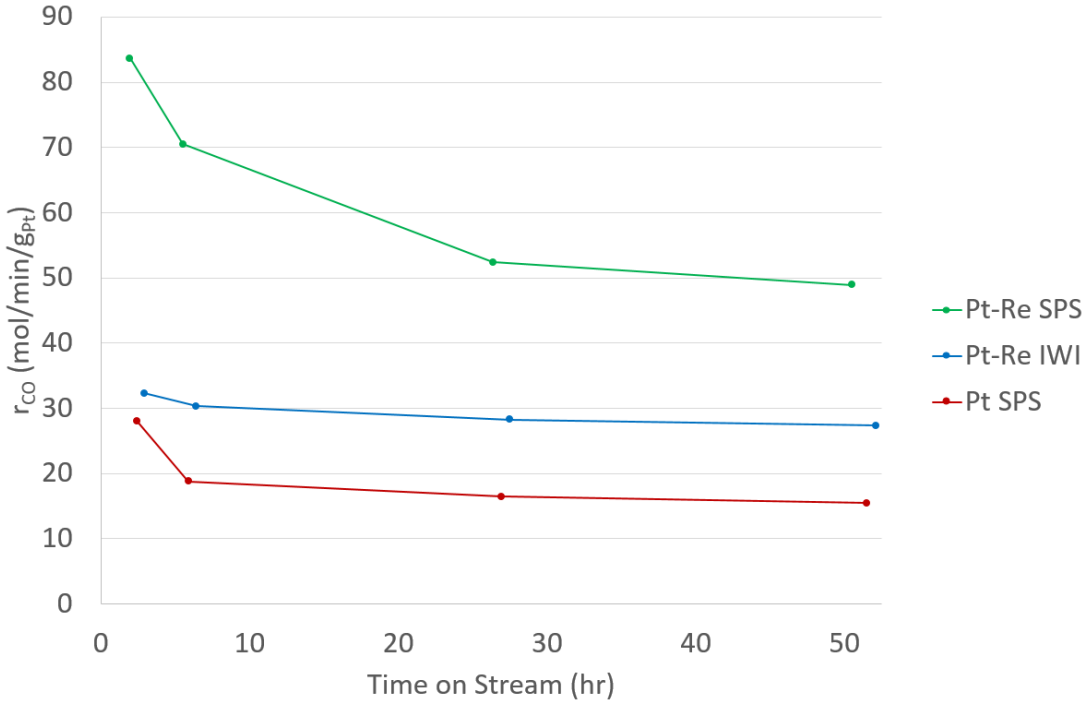

Figure 8.1: Activity and stability of the catalysts evaluated at 320 °C, normalised to Pt metal mass

The rate of carbon monoxide consumed normalised to the mass of Pt present in the catalyst was used to determine the activity of each catalyst. The initial activity and the change in activity with time on stream (ToS) are shown in figure 8.1. The initial activity shows that the addition of rhenium promotes the rate of the WGS reaction irrespective of which preparation method is used. The extent to which the rate is improved does depend on the preparation method however, as the Pt-Re/CeO_2 catalyst prepared by SPS had an initial CO consumption of 83 mol/min/g_{Pt}, while the catalyst prepared by IWI had a CO consumption of 32 mol/min/g_{Pt}, representing a 2.6x improvement in initial performance.

The catalysts were then kept on stream for long enough to observe deactivation. The deactivation is most apparent in the Pt-Re catalyst synthesised by SPS, losing 42 % of its initial activity over the course of the run. The platinum catalyst had a quick loss of activity initially, losing 33 % over 3.5 hours but then stabilised, losing 17 % of the activity, measured at 3.5 hours, over the next 45 hours. The Pt-Re catalyst synthesised by IWI was the most stable of all the catalysts over the course of the run, steadily losing 16 % of its initial activity over entire run.

The deactivation behaviour of the Pt catalyst, also synthesised by SPS, agrees with what Choung *et al.* (2005) reported at 300 °C, which was an initial activity loss of 40 % over 20 hours followed by a 5 % loss in activity over 40 hours. Choung *et al.* (2005) used a Pt catalyst on a mixed ceria-zirconia support synthesised by IWI as well, so the synthesis method used does not affect the deactivation behaviour of the pure Pt catalyst.

The synthesis method used does affect the stability of the Pt-Re catalysts at 320 °C, with the SPS synthesis method losing more activity than the IWI method. The difference in stability could be due to the amount of Re present on each catalyst, as there was less Re in the SPS synthesised catalyst than in the IWI synthesised catalyst, either by weight or Pt:Re ratio.

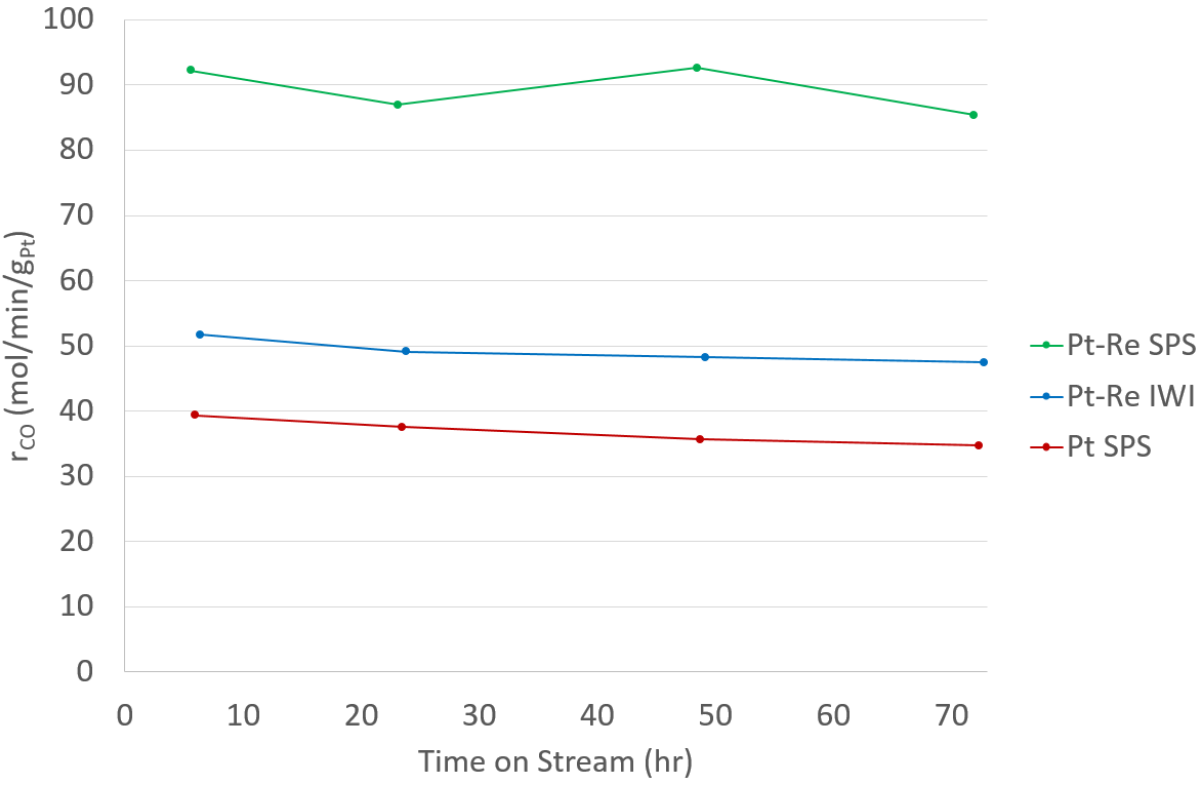

Figure 8.2: Activity and stabiltiy of the catalysts evaluated at 350 °C, normalised to Pt metal mass

The activity for each catalyst was then evaluated at 350 °C, and is shown in figure 8.2. Similarly to the evaluation conducted at 320 °C, the Pt-Re catalysts had higher activity than the Pt catalyst. The Pt-Re catalyst synthesised by SPS still outperformed the Pt-Re catalyst prepared by IWI. All of the catalysts displayed the expected increase in activity with temperature, however this was uneven across the catalysts, with the Pt-Re IWI catalyst showing a greater increase than the other two catalysts.

The deactivation behaviour of the Pt-Re IWI catalyst at 350 °C is similar to that at 320 °C, and so the mechanism of deactivation should be similar. The Pt catalyst shows a gradual deactivation over the course of the run, with no initial fast deactivation happening, unlike its behaviour at 320 °C. The Pt-Re SPS catalyst also shows a change in deactivation behaviour, being more stable at 350 °C than at 320 °C. The catalysts prepared by SPS becoming more stable at a higher temperature indicates that there is a change in the mechanism of deactivation between 320 and 350 °C, and that it is potentially dependent on the synthesis method. The exact cause is difficult to determine from these data however, and more experimentation is required. These experiments would require more performance over a wider range of temperatures, along with different gas concentrations, to see if the catalyst is deactivated via poisoning, support changes, particle growth or other routes. The catalysts could also be evaluated at different conversions, as this might also be a factor in the deactivation.

8.2 Post-Run Characterisation

The catalysts were then characterised using TEM to see if any changes could be found after having been under WGS conditions for an extended duration.

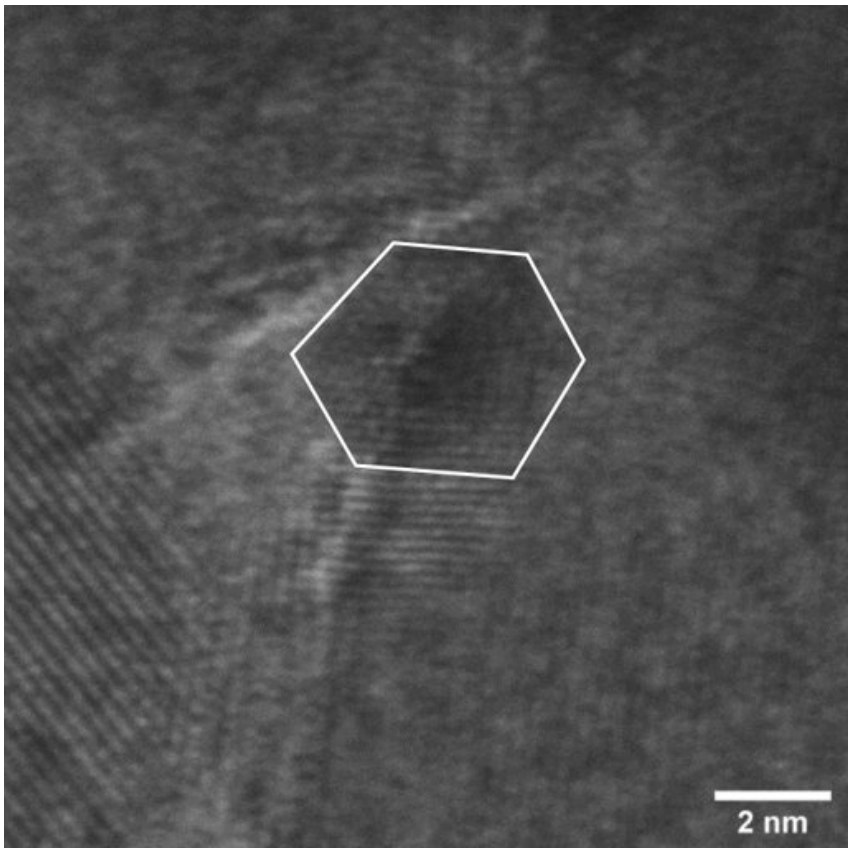

Figure 8.3: Platinum nanoparticle (white outline) supported on ceria.

Figure 8.3 shows a Pt nanoparticle from the Pt/CeO_2 (SPS) catalyst after being evaluated at 320 °C. The white outline indicates that the particle projects a well-defined hexagonal shape. This is different to the rounded shapes that the freshly synthesised Pt nanoparticles had (cf. figure 6.2). This facetted shape is found in the *operando* TEM work at 320 ° C, showing that the nanoparticles will change shape during operation when supported on CeO_2. However this is only one nanoparticle found on the catalyst, and other nanoparticles could be different shapes.

In contrast to the facetted shape of the Pt nanoparticle, a Pt-Re nanoparticle was found in the $Pt\text{-}Re/CeO_2$ catalyst synthesised by SPS to have a spherical shape. This particle is shown in figure 8.4.

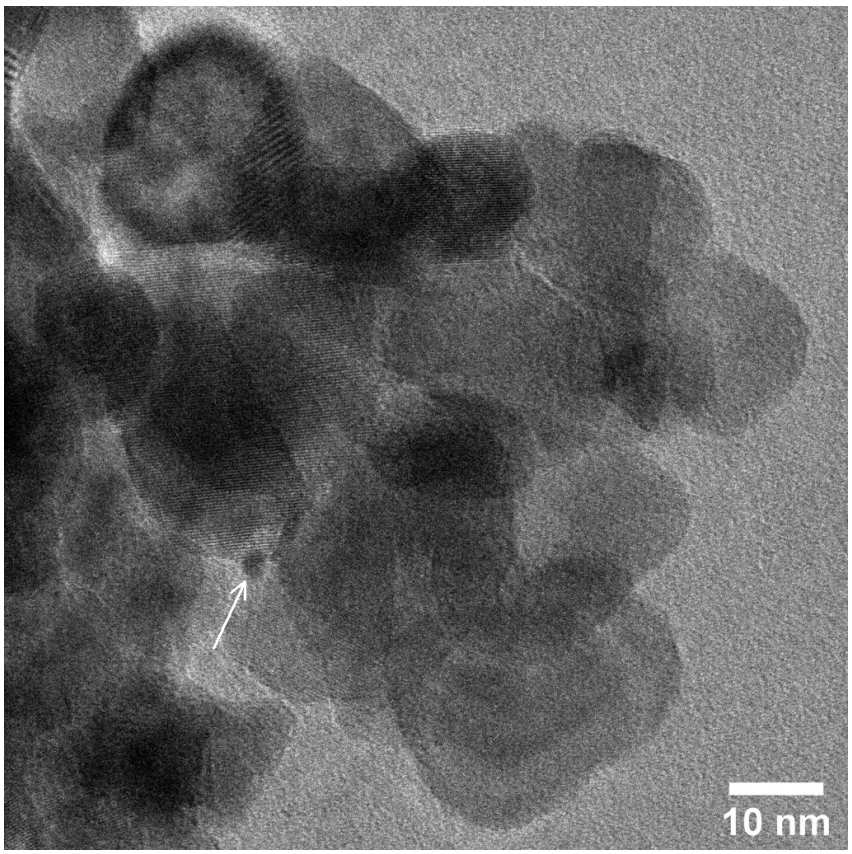

Figure 8.4: Spherical Pt-Re (SPS) nanoparticle (arrow) supported on ceria after reaction at 320 °C

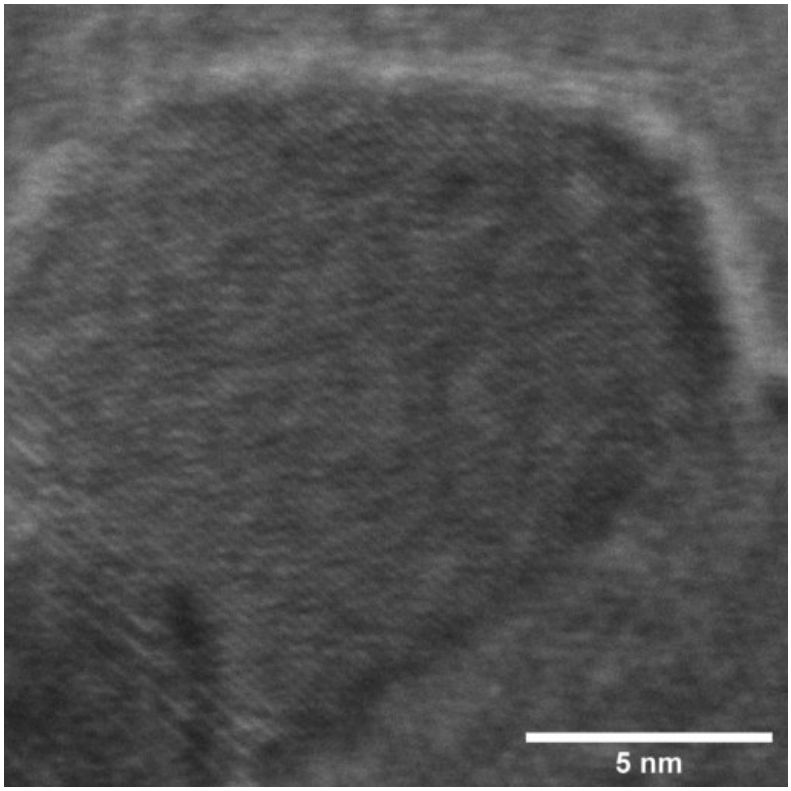

Figure 8.5: Facetted Pt-Re nanoparticle in Pt-Re IWI catalyst after reaction at 320 °C

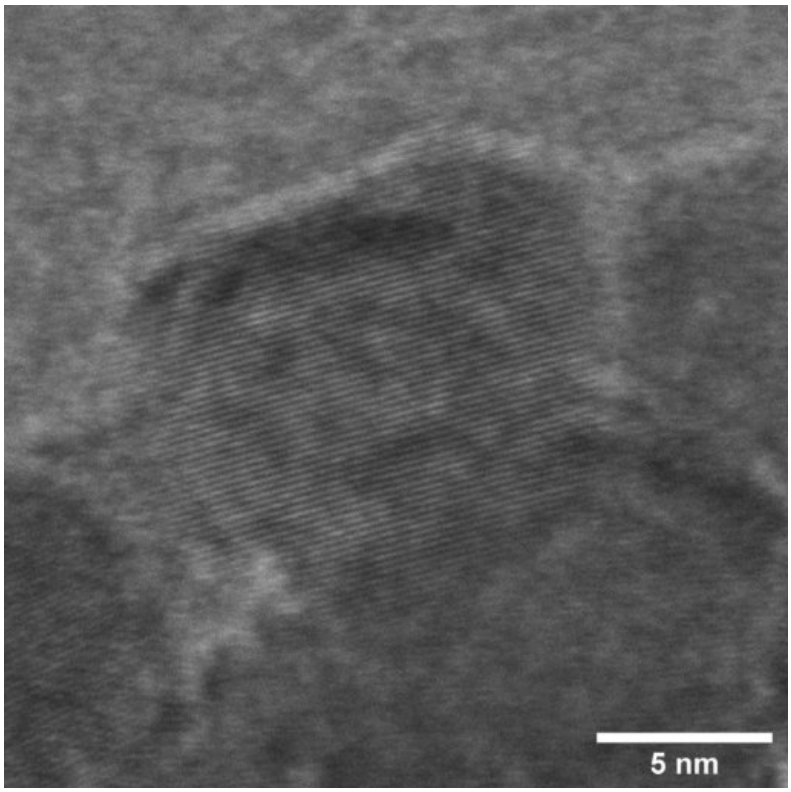

Figure 8.6: Different facetted Pt-Re nanoparticle in Pt-Re IWI catalyst after reaction at 320 °C

Figures 8.5 and 8.6 show two different metal nanoparticles of the Pt-Re/CeO_2 catalyst prepared by IWI. Both nanoparticles are facetted, but with different shapes, however other nanoparticles on the catalyst probably have different shapes to these two as well. This is similar to the *operando* work, where the same unsupported nanoparticle returned to a facetted shaped that was different from the previous facetted shape. However, this occurs on two different nanoparticles that are supported on ceria, so the metal-support interaction (if any) could be affecting the shapes.

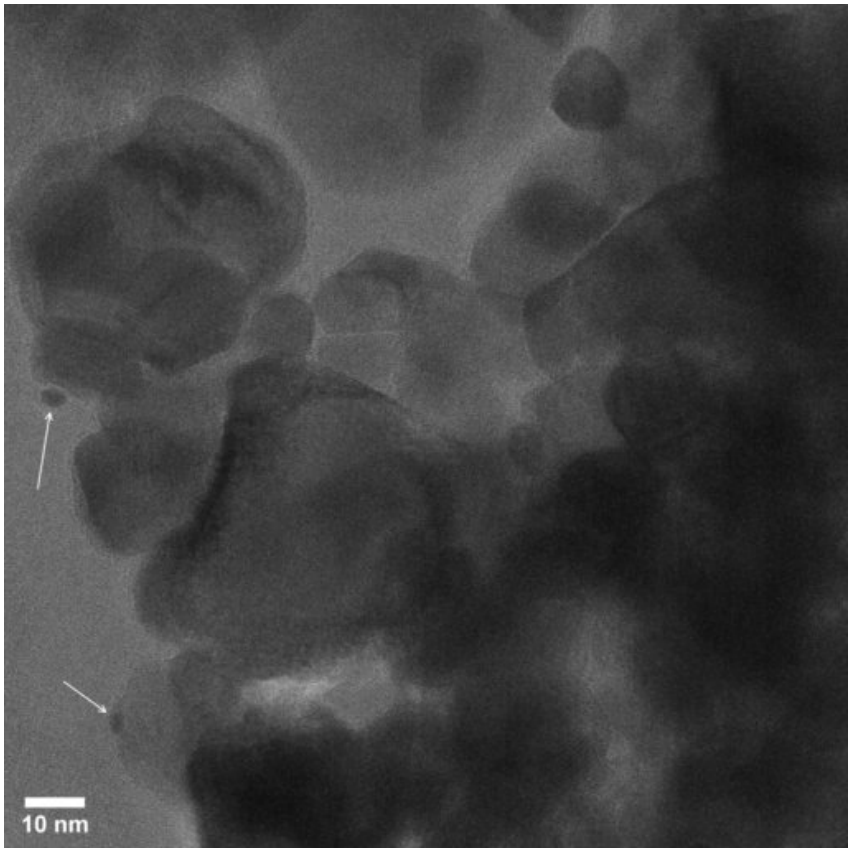

Figure 8.7: Pt nanoparticles (white arrows) on ceria after being evaluated at 350 °C

Figure 8.7 shows two platinum nanoparticles supported on ceria after reaction at 350 °C. The larger, higher nanoparticle has a facetted shape compared to the smaller more spherical nanoparticle lower down in the figure. Two nanoparticles on the same catalyst having different shapes shows that these oscillations are not synchronous across the catalyst. Thus, any effect they have on the WGS reaction rate would only be seen as an average.

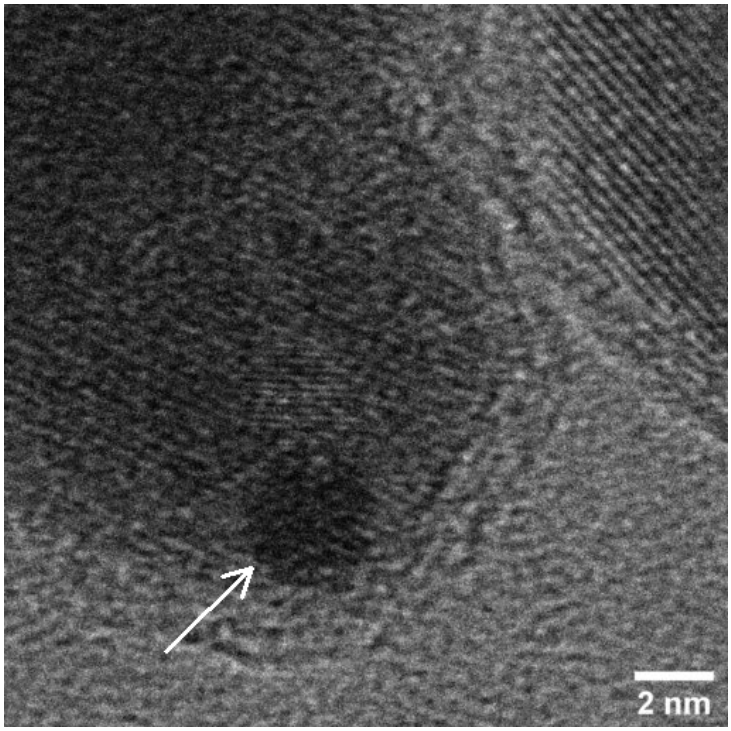

Figure 8.8: Pt nanoparticle on ceria after being evaluated at 350 °C

Figure 8.8 shows a spherical Pt nanoparticle on ceria, indicated by the arrow. Around the ceria is an amorphous layer, which did not grow over time spent under the electron beam, as any remaining surfactants present on the catalyst are removed during reduction and reactor start-up. This indicates that the layer was formed during reaction and could be a cause for deactivation. The layer is most likely carbon, as its contrast with the carbon film of the TEM grid is minimal.

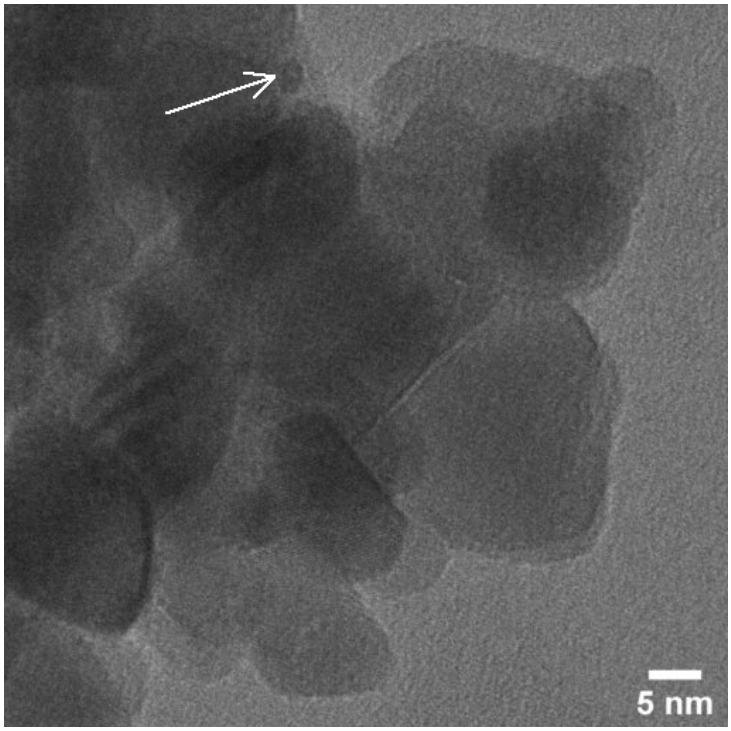

Figure 8.9: Pt-Re (SPS) nanoparticle on ceria after being evaluated at 350 °C

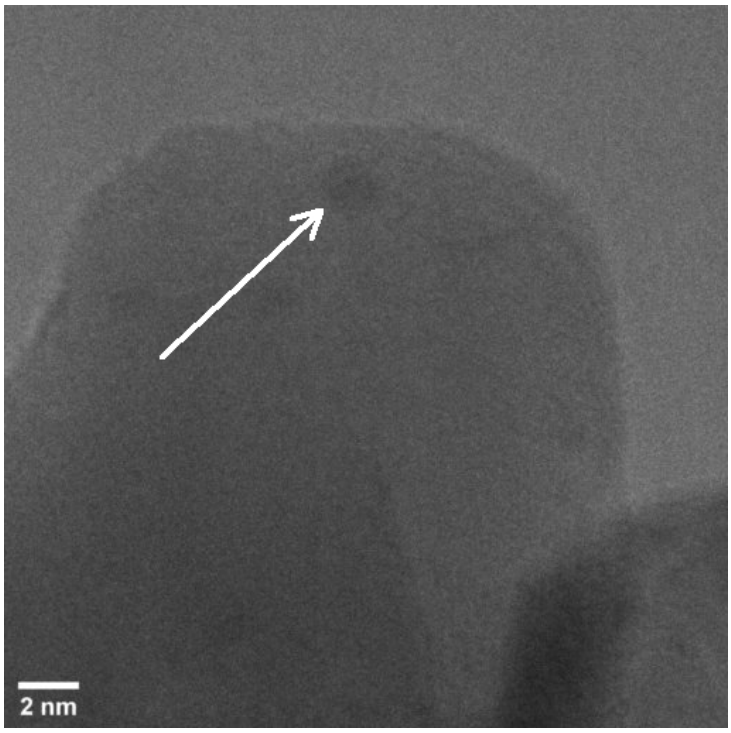

Figure 8.10: Pt-Re (IWI) nanoparticle on ceria after being evaluated at 350 °C

The Pt-Re nanoparticle in figure 8.9 was prepared by SPS and is facetted, while the nanoparticle shown in figure 8.10 was prepared by IWI, the shape of which is difficult to determine as the contrast is low.

Across all temperatures, method of preparation, and promotion, the metal nanoparticles ex-

hibited both spherical and facetted shapes. Whether a particle was spherical or facetted does not seem to correlate with temperature or nanoparticle composition. Therefore, it is likely that the formation of facets is an inherent property of platinum nanoparticles in a WGS reaction active environment. As was said in the *operando* section, which specific gas and/or temperature causes this shape change still needs to be determined.

Chapter 9

Conclusions and Recommendations

In conclusion, platinum, as well as platinum-rhenium nanoparticles were successfully synthesised using the SPS method. This method was then optimised from literature to produce smaller nanoparticles with an average size between 2.7 - 3.8 nm and a monodisperse particle size distribution. Alloying of the platinum-rhenium particles could not be confirmed.

The nanoparticles were then supported on ceria, however ICP-OES revealed that the total metal loading was lower than anticipated. The ICP-OES results also showed that the amount of Re present in the nanoparticles synthesised by SPS was much less than was targeted, therefore a majority of the Re is lost during synthesis. The low yield of the SPS method is attributed to the shorter aging time of 10 min and the lower temperature of 160 °C compared to the literature method. A Pt-Re/CeO_2 catalyst synthesised by IWI was confirmed by ICP-OES to have a metal loading of 1.05 wt %, although the targeted ratio of Pt to Re (3:1) was not achieved, with the actual Pt to Re ratio being 1.7:1. XRD was unable to detect any of the metal nanoparticles present on the catalyst due to the low metal loading and small particle size. Characterisation of the supported catalysts by TEM was very difficult due to the low Z number contrast between ceria, platinum and rhenium.

Using *operando* TEM, the behaviour of the Pt and Pt-Re nanoparticles under water gas shift reaction conditions was observed. The nanoparticles displayed oscillations between a facetted shape and a spherical shape. These oscillations occurred at 320 and at 350 °C, for both the Pt and Pt-Re nanoparticles. These oscillations are not seen in vacuum under normal TEM imaging conditions. Therefore, the oscillations are caused by the presence of the reactive gases and elevated temperature, however the exact cause of the oscillations is not yet known.

The evaluation of the catalysts at a lab scale confirmed the hypothesis that the Pt-Re/CeO_2 catalyst synthesised by SPS had a higher activity than the Pt-Re/CeO_2 synthesised by IWI. The Pt-Re catalyst synthesised by SPS also made more efficient use of the rhenium present than the catalyst synthesised by IWI. The stability of the Pt-Re catalyst synthesised by SPS at 320 °C was much lower than the Pt-Re catalyst synthesised by IWI, therefore the preparation method does have an effect on stability at this temperature. At 350 °C however, the Pt-Re catalyst synthesised by SPS was much more stable, and so was the Pt catalyst. Therefore there is a deactivation mechanism occurring at 320 °C that is not present at 350 °C.

TEM characterisation of the catalysts after undergoing catalytic performance evaluation revealed that some metal nanoparticles had facetted shapes when on the ceria support. The metal nanoparticles synthesised by SPS were mostly spherical, thus this change occurred during the reaction. Therefore, the refacetting behaviour of the metal nanoparticles observed under *operando* TEM also occurs under lab scale reaction conditions on metal-oxide supports.

To further explore this line of investigation, recommendations include:

- Further optimisation of the SPS method to improve yield and amount of rhenium alloyed, using a different method to synthesise colloidal Pt-Re nanoparticles if necessary.
- Support the catalysts on TiO_2 to enable easier characterisation under TEM, and potential activity increases compared to using CeO_2.
- Use different TEM/STEM techniques, such as High-Angle Annular Dark Field (HAADF) imaging, to allow easier characterisation of the catalyst.
- More experiments using *operando* TEM, by loading the metal onto a metal-oxide support.
- Changing the concentrations of the gases used in *operando* TEM, as well as the temperatures to observe the effects on the catalyst.
- Using the RGA during *operando* TEM to see what effects the oscillations have on the WGS reaction rate.
- Evaluating the activity and stability of the catalysts at different temperatures and conversions to try and determine the cause for the change in deactivation behaviour.
- Temperature Programmed Desorption, using a CO probe molecule, to determine changes to the heat of adsorption of CO on Pt with the addition of Re.
- X-Ray Photoelectron Spectroscopy of the catalysts before and after reaction to help determine phases present in the catalyst.
- Using electrochemistry, especially the cyclic voltammetry technique in the 0 to 1.0 V range, as the shift in redox peaks from pure Pt would also help to show Pt-Re alloying.

Bibliography

Azzam, K.G., Babich, I.V., Seshan, K., & Lefferts, L. 2007. Bifunctional catalysts for single-stage water–gas shift reaction in fuel cell applications. Part 1. Effect of the support on the reaction sequence. *Journal of Catalysis*, 251(1):153–162.

Azzam, K.G., Babich, I.V., Seshan, K., & Lefferts, L. 2008. Role of Re in Pt–Re/TiO_2 catalyst for water gas shift reaction: A mechanistic and kinetic study. *Applied Catalysis B: Environmental*, 80:129–140.

Bartels, J.R., Pate, M.B., & Olson, N.K. 2010. An economic survey of hydrogen production from conventional and alternative energy sources. *International Journal of Hydrogen Energy*, 35:8371–8384.

Bunluesin, T., Gorte, R., & Graham, G. 1998. Studies of the water-gas-shift reaction on ceria-supported Pt, Pd, and Rh: Implications for oxygen-storage properties. *Applied Catalysis B: Environmental*, 15(1-2):107–114.

Choung, S.Y., Ferrandon, M., & Krause, T. 2005. Pt-Re bimetallic supported on CeO_2-ZrO_2 mixed oxides as water-gas shift catalysts. *Catalysis Today*, 99(3-4):257–262.

Creemer, J., Helveg, S., Hoveling, G., Ullmann, S., Molenbroek, A., Sarro, P., & Zandbergen, H. 2008. Atomic-scale electron microscopy at ambient pressure. *Ultramicroscopy*, 108(9):993–998.

Creemer, J., Santagata, F., Morana, B., Mele, L., Alan, T., Iervolino, E., Pandraud, G., & Sarro, P. 2011. An all-in-one nanoreactor for high-resolution microscopy on nanomaterials at high pressures. In *2011 IEEE 24th International Conference on Micro Electro Mechanical Systems*, pages 1103–1106. IEEE.

Del Villar, V., Barrio, L., Helmi, A., Annaland, M.V.S., Gallucci, F., Fierro, J.L., & Navarro, R.M. 2016. Effect of Re addition on the WGS activity and stability of Pt/CeO_2-TiO_2 catalyst for membrane reactor applications. *Catalysis Today*, 268:95–102.

Ertl, G., Knözinger, H., & Weitkamp, J. 1997. *Handbook of heterogeneous catalysis*. Wiley-VCH.

Gonzalez Castaño, M., Reina, T., Ivanova, S., Centeno, M., & Odriozola, J. 2014. Pt vs. Au in water–gas shift reaction. *Journal of Catalysis*, 314:1–9.

Jensen, E. & Mølhave, K. 2016. *Encapsulated Liquid Cells for Transmission Electron Microscopy*, pages 35–55. Advances in Microscopy and Microanalysis. Cambridge University Press.

Kalamaras, C.M., Americanou, S., & Efstathiou, A.M. 2011. "Redox" vs "associative formate with -OH group regeneration" WGS reaction mechanism on Pt/CeO_2: Effect of platinum particle size. *Journal of Catalysis*, 279(2):287–300.

Kothari, R., Buddhi, D., & Sawhney, R.L. 2008. Comparison of environmental and economic aspects of various hydrogen production methods. *Renewable and Sustainable Energy Reviews*, 12(2):553–563.

Kruger, D. 2019. *Gas phase heterogeneous catalyst performance testing in laboratory fixed-bed reactors.* Master's thesis, University of Cape Town.

Mueller-Langer, F., Tzimas, E., Kaltschmitt, M., & Peteves, S. 2007. Techno-economic assessment of hydrogen production processes for the hydrogen economy for the short and medium term. *International Journal of Hydrogen Energy*, 32:3797–3810.

Munnik, P., De Jongh, P.E., & De Jong, K.P. 2015. Recent Developments in the Synthesis of Supported Catalysts. *Chemical Reviews*, 115(14):6687–6718.

Niemantsverdriet, J. 2007. *Spectroscopy in Catalysis: An Introduction*. Wiley.

Ponec, V. & Bond, G. 1995. *Catalysis by metals and alloys*. Elsevier.

Raciti, D., Kubal, J., Ma, C., Barclay, M., Gonzalez, M., Chi, M., Greeley, J., More, K.L., & Wang, C. 2016. Pt_3Re alloy nanoparticles as electrocatalysts for the oxygen reduction reaction. *Nano Energy*, 20:202–211.

Radhakrishnan, R., Willigan, R., Dardas, Z., & Vanderspurt, T. 2006. Water gas shift activity and kinetics of Pt/Re catalysts supported on ceria-zirconia oxides. *Applied Catalysis B: Environmental*, 66(1-2):23–28.

Rubin, E.S., Mantripragada, H., Marks, A., Versteeg, P., & Kitchin, J. 2012. The outlook for improved carbon capture technology. *Progress in Energy and Combustion Science*, 38(5):630–671.

van Santen, R.A. 2009. Insensitive Catalytic Relationships. *Accounts of Chemical Research*, 42(1):57–66.

Sato, Y., Terada, K., Hasegawa, S., Miyao, T., & Naito, S. 2005. Mechanistic study of water-gas-shift reaction over TiO_2 supported Pt-Re and Pd-Re catalysts. *Applied Catalysis A: General*, 296:80–89.

Sato, Y., Terada, K., Soma, Y., Miyao, T., & Naito, S. 2006. Marked addition effect of Re upon the water gas shift reaction over TiO_2 supported Pt, Pd and Ir catalysts. *Catalysis Communications*, 7:91–95.

Vendelbo, S.B., Elkjær, C.F., Falsig, H., Puspitasari, I., Dona, P., Mele, L., Morana, B., Nelissen, B.J., Van Rijn, R., Creemer, J.F., Kooyman, P.J., & Helveg, S. 2014. Visualization of oscillatory behaviour of Pt nanoparticles catalysing CO oxidation. *Nature Materials*, 13(9):884–890.

Vignatti, C., Avila, M.S., Apesteguía, C.R., & Garetto, T.F. 2010. Catalytic and DRIFTS study of the WGS reaction on Pt-based catalysts. *International Journal of Hydrogen Energy*, 35(14):7302–7312.

Williams, D.B. & Carter, C.B. 2009. *Transmission Electron Microscopy: A Textbook for Materials Science*. Springer, 2nd edition.

Yoshida, H., Matsuura, K., Kuwauchi, Y., Kohno, H., Shimada, S., Haruta, M., & Takeda, S. 2011. Temperature-Dependent Change in Shape of Platinum Nanoparticles Supported on CeO_2 during Catalytic Reactions. *Applied Physics Express*, 4(6):065001–3.

Appendix A

Calibrations

A.1 Mass Flow Controllers

The MFCs were calibrated for the relationship between gas flow rate and set-point value using a straight line with an intercept of zero. The gradient shown in tables A.1 and A.2 (obtained via linear regression), multiplied by the set-point value will give the STP gas flow rate.

Table A.1: Calibration data for MFCs controlling the inlet gas mixture.

Inlet Gas	Gradient
Nitrogen	1.03
Carbon dioxide	0.985
Carbon monoxide	1.40
Hydrogen	1.09

Table A.2: Calibration data for MFCs controlling the mixed dry gas inlet to the reactors.

Reactor	Gradient
1	0.976
2	0.968
3	0.962

A.2 Gas Chromatography

Four different gas mixtures were used to calibrate the GC response to changes in gas composition, and are given in table A.3:

Table A.3: Composition of gas mixtures used to calibrate the GC

Gas	Mix 1 (%)	Mix 2 (%)	Mix 3 (%)	Mix 4 (%)
Carbon monoxide	11	9	7	13
Carbon dioxide	13	11	9	17
Nitrogen	21	10	9	25
Hydrogen	55	70	75	45

The area under the peak of each identified gas, in μV·s, is proportional to the concentration of that gas. The area response to a concentration of gas was fitted to a straight line with an

intercept of zero. The gas concentration multiplied by the gradient gives the area under the peak, so the inverse can be used to determine the concentration when the peak area is known.

Table A.4: Calibration data for the GC response to gas concentrations

Gas	Channel	Gradient
Hydrogen	1	99714
Nitrogen	1	13257
Nitrogen	2	8028
Carbon monoxide	1	13729
Carbon monxoide	2	8063
Carbon dioxide	4	24263

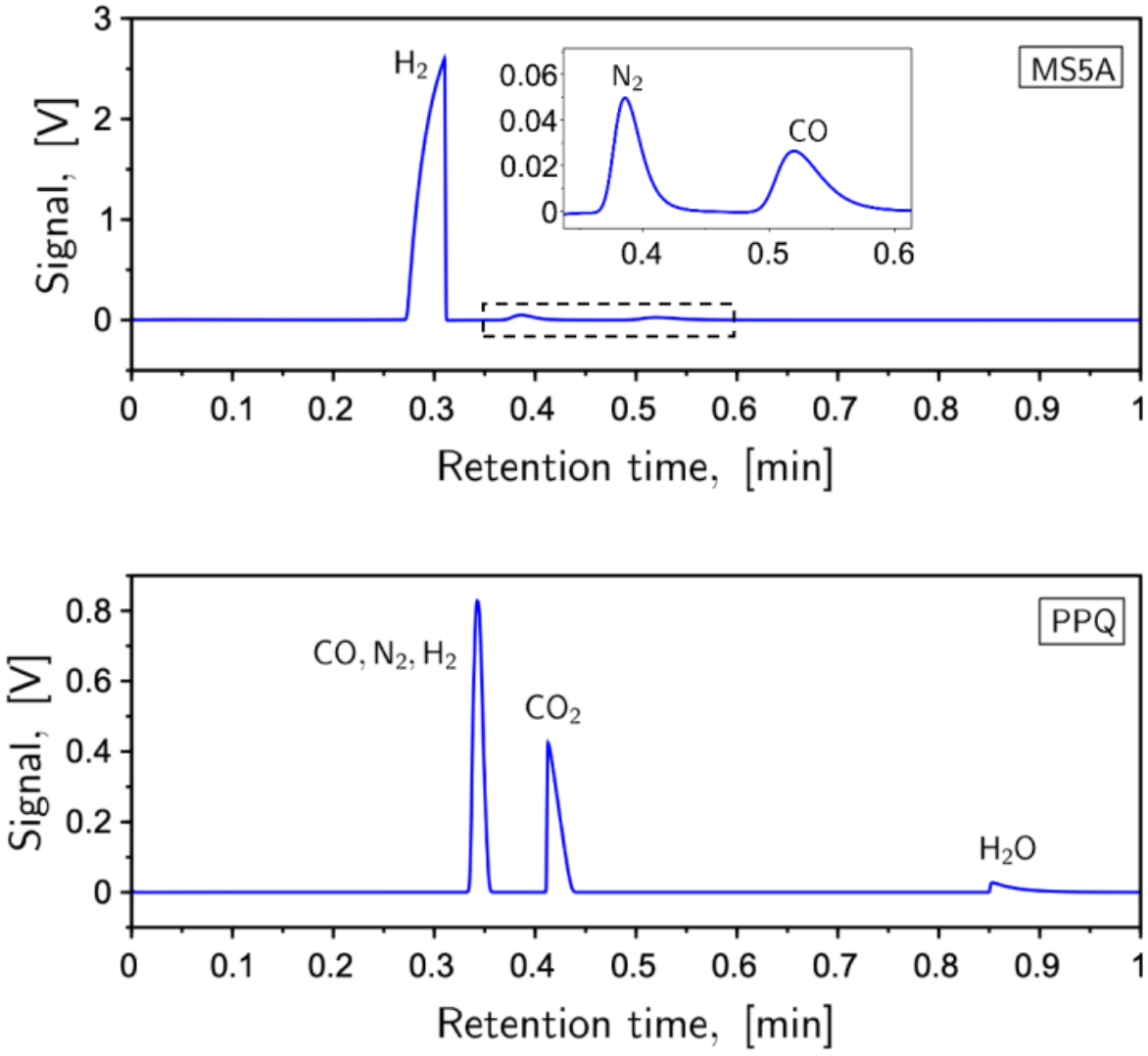

Figure A.1: Example chromatogram of dry reactor outlet gas (Kruger, 2019)

Appendix B

Particle Size Distribution Plots

This appendix contains the particle size distribution plots for each of the points in figure 5.3.

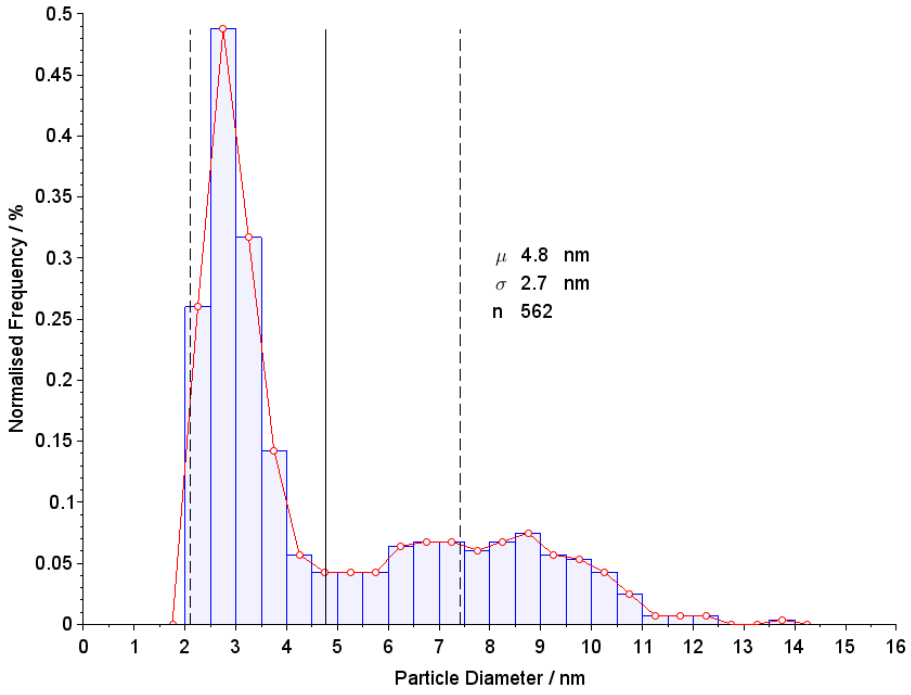

Figure B.1: PSD of Pt-Re nanoparticles aged for 30 min at 120 °C

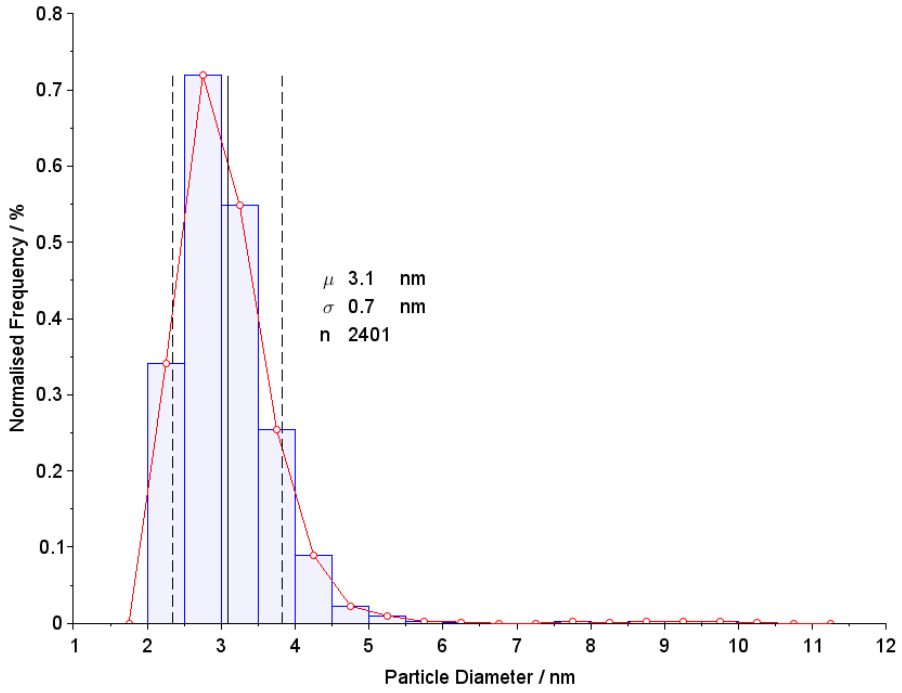

Figure B.2: PSD of Pt-Re nanoparticles aged for 90 min at 120 °C

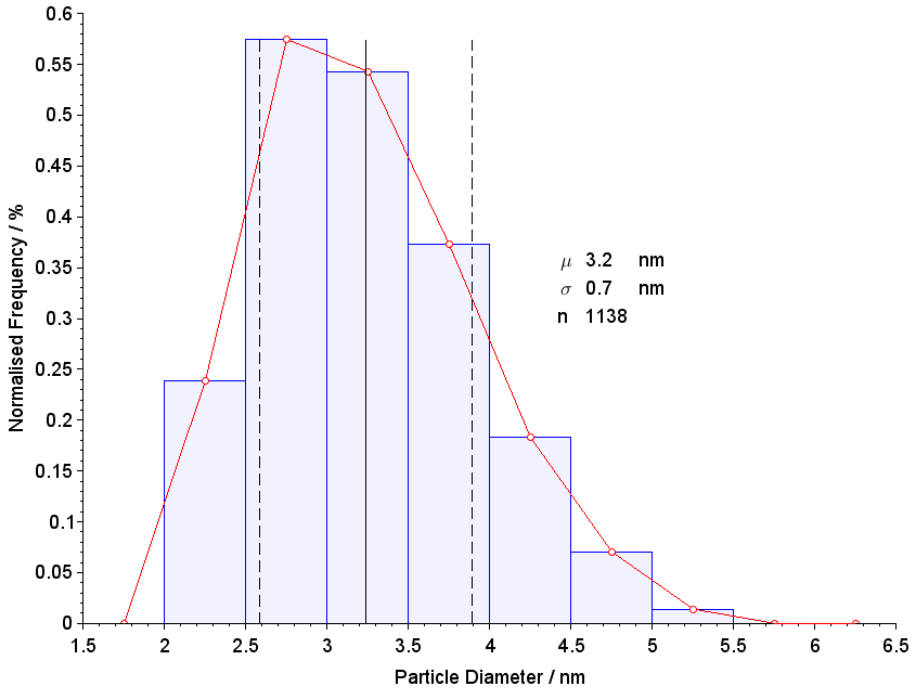

Figure B.3: PSD of Pt-Re nanoparticles aged for 150 min at 120 °C

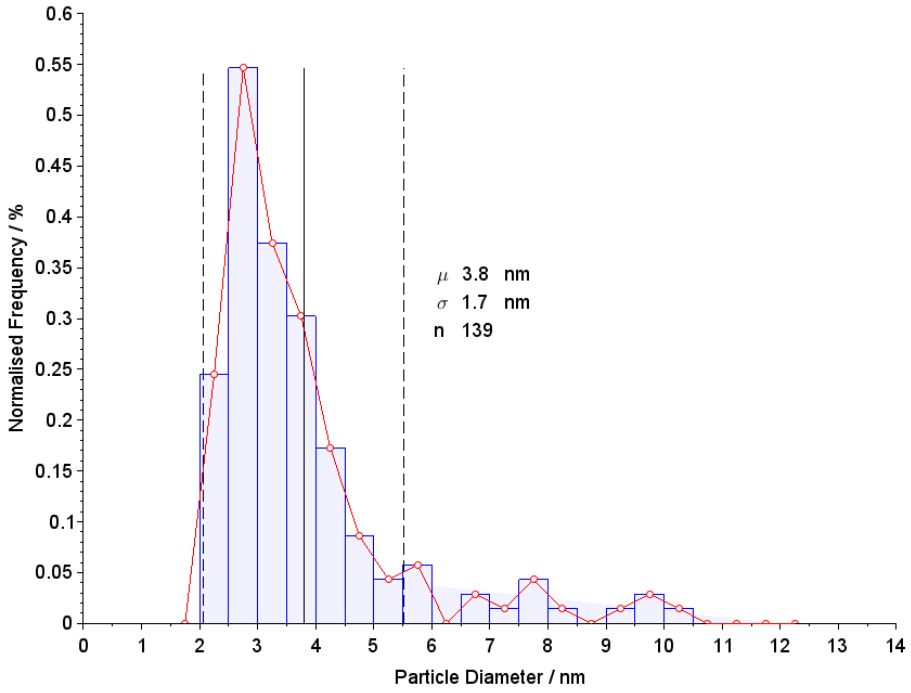

Figure B.4: PSD of Pt-Re nanoparticles aged for 15 min at 140 °C

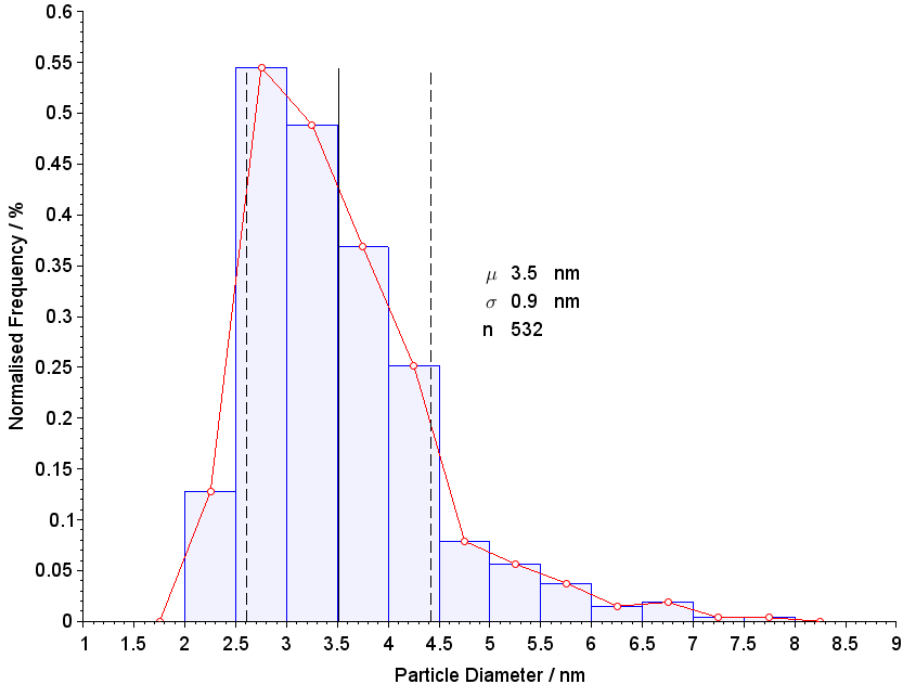

Figure B.5: PSD of Pt-Re nanoparticles aged for 30 min at 140 °C

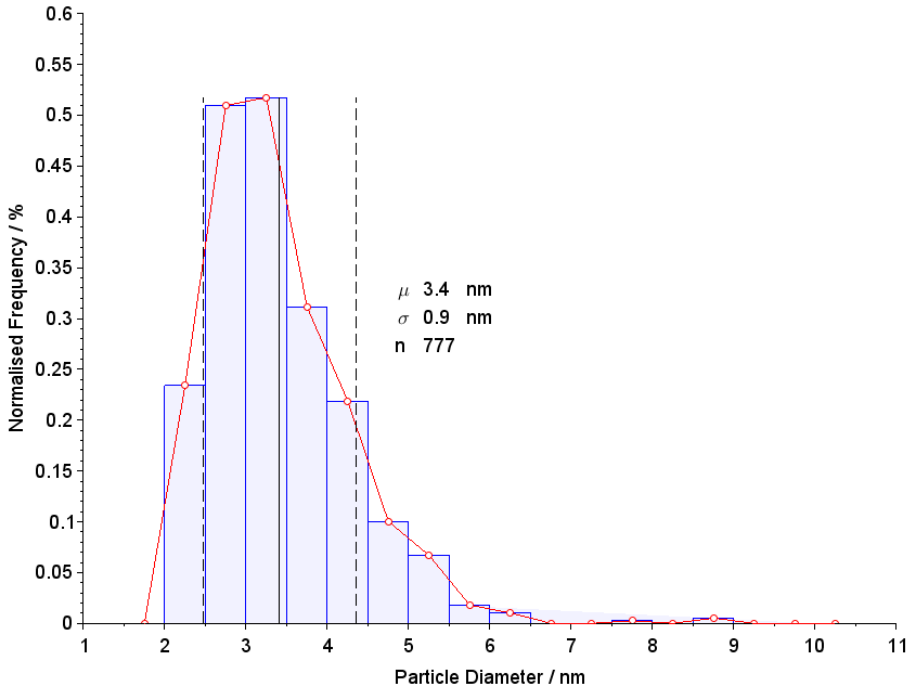

Figure B.6: PSD of Pt-Re nanoparticles aged for 45 min at 140 °C

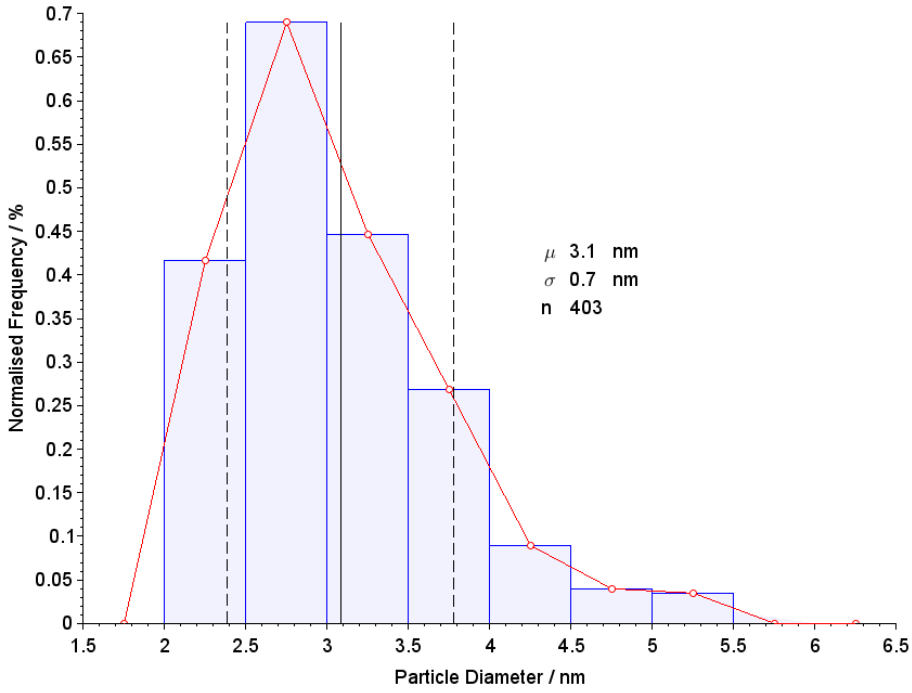

Figure B.7: PSD of Pt-Re nanoparticles aged for 60 min at 140 °C

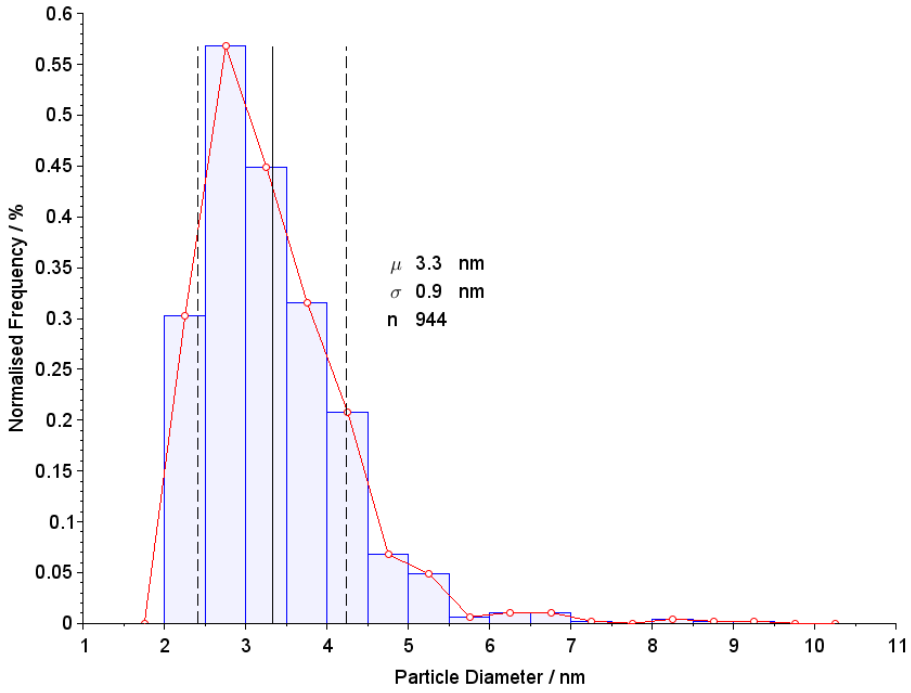

Figure B.8: PSD of Pt-Re nanoparticles aged for 10 min at 160 °C

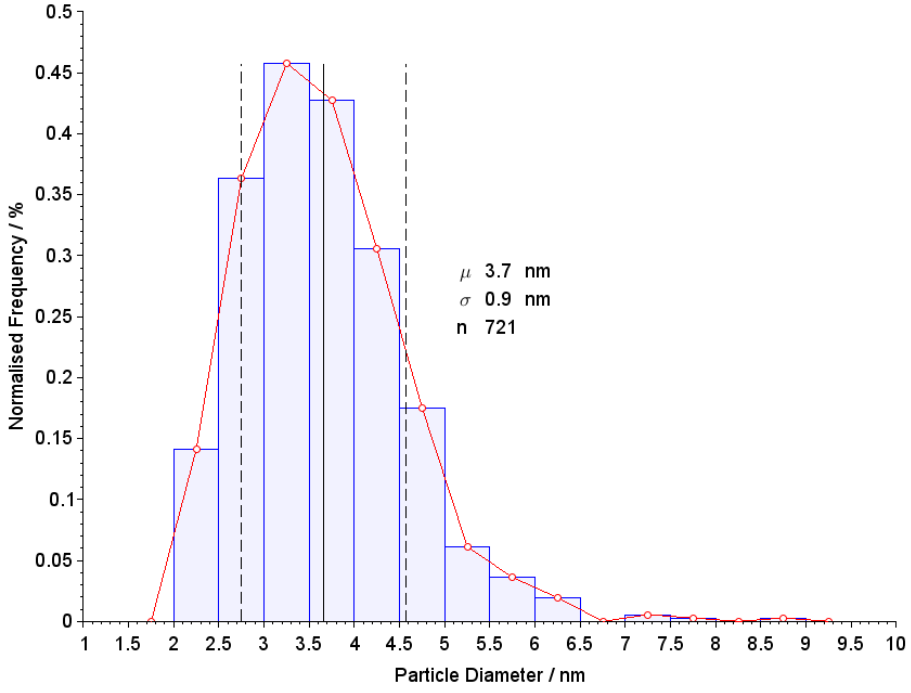

Figure B.9: PSD of Pt-Re nanoparticles aged for 20 min at 160 °C

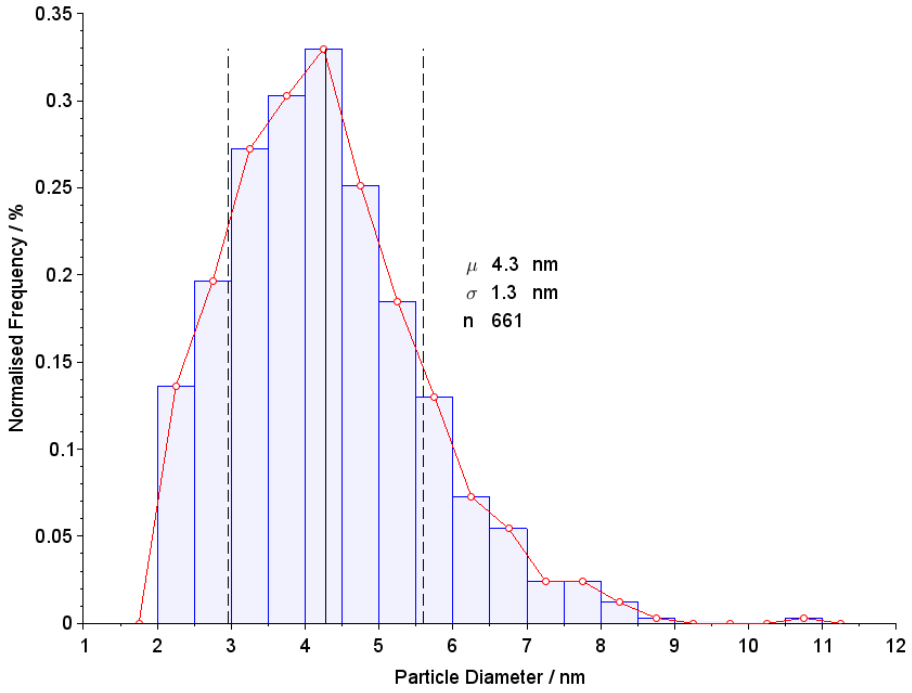

Figure B.10: PSD of Pt-Re nanoparticles aged for 30 min at 160 °C

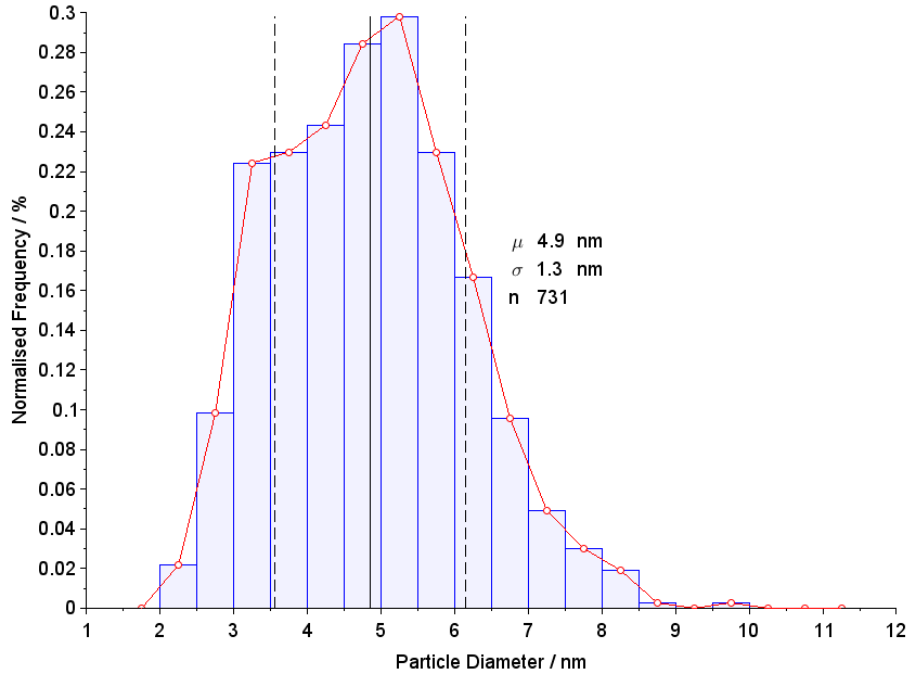

Figure B.11: PSD of Pt-Re nanoparticles aged for 40 min at 160 °C